JGR Oceans

RESEARCH ARTICLE
10.1029/2020JC017026

Enhanced Turbulence in the Upper Mixed Layer Under Light Winds and Heating: Implications for Gas Fluxes

Sally MacIntyre[1,2,3], J. H. F. Amaral[3], and J. M. Melack[1,3]

[1]Department of Ecology, Evolution and Marine Biology, University of California, Santa Barbara, CA, USA, [2]Marine Science Institute, University of California, Santa Barbara, CA, USA, [3]Earth Research Institute, University of California, Santa Barbara, CA, USA

Key Points:

- Dissipation rates (ε) in the upper 0.25 m of a tropical water body reached 10^{-5} m^2 s^{-3} under light winds and heating
- For winds up to 3.5 m s^{-1}, ε depended on heating rather than wind speed, and ε was 10 times higher under heating than cooling
- Gas transfer velocities were four times higher under light winds and heating than predicted from wind-based models

Supporting Information:

Supporting Information may be found in the online version of this article.

Correspondence to:

S. MacIntyre,
sally@eri.ucsb.edu

Citation:

MacIntyre, S., Amaral, J. H. F., & Melack, J. M. (2021). Enhanced turbulence in the upper mixed layer under light winds and heating: Implications for gas fluxes. *Journal of Geophysical Research: Oceans*, *126*, e2020JC017026. https://doi.org/10.1029/2020JC017026

Received 28 NOV 2020
Accepted 29 NOV 2021

Author Contributions:

Conceptualization: Sally MacIntyre, J. M. Melack
Data curation: Sally MacIntyre
Formal analysis: Sally MacIntyre, J. H. F. Amaral
Funding acquisition: Sally MacIntyre, J. M. Melack
Investigation: Sally MacIntyre, J. H. F. Amaral, J. M. Melack
Methodology: Sally MacIntyre, J. H. F. Amaral, J. M. Melack
Project Administration: Sally MacIntyre, J. M. Melack
Resources: Sally MacIntyre, J. M. Melack

Abstract Measurements of turbulence, as rate of dissipation of turbulent kinetic energy (ε), adjacent to the air-water interface are rare but essential for understanding of gas transfer velocities (k) used to compute fluxes of greenhouse gases. Variability in ε is expected over diel cycles of stratification and mixing. Monin-Obukhov similarity theory (MOST) predicts an enhancement in ε during heating (buoyancy flux, β^+) relative to that for shear ($u_{*_w}{}^3/\kappa z$ where u_{*_w} is water friction velocity, κ is von Karman constant, z is depth). To verify and expand predictions, we quantified ε in the upper 0.25 m and below from profiles of temperature-gradient microstructure in combination with time series meteorology and temperature in a tropical reservoir for winds <4 m s^{-1}. Maximum likelihood estimates of near-surface ε during heating were independent of wind speed and high, ~5×10^{-6} m^2 s^{-3}, up to three orders of magnitude higher than predictions from $u_{*_w}{}^3/\kappa z$, increased with heating, and were ~10 times higher than during cooling. k, estimated using near-surface ε, was ~10 cm hr^{-1}, validated with k obtained from chamber measurements, and 2–5 times higher than computed from wind-based models. The flux Richardson number (R_f) varied from ~0.4 to ~0.001 with a median value of 0.04 in the upper 0.25 m, less than the critical value of 0.2. We extend MOST by incorporating the variability in R_f when scaling the influence of β^+ relative to $u_{*_w}{}^3/\kappa z$ in estimates of ε, and by extension, k, obtained from time series meteorological and temperature data.

Plain Language Summary Fluxes of climate forcing trace gases in aquatic systems depend on physical processes, specifically turbulence for light to moderate winds, and the concentration gradient at the air-water interface. The physical processes can be represented as a gas transfer velocity (k). We analyze physical and biogeochemical data from a tropical reservoir and provide an algorithm for computing near-surface turbulence, as rate of dissipation of turbulent kinetic energy (ε), and k during heating and light winds, as commonly occur during morning in both lakes and oceans and during heat waves at all latitudes. During heating when wind speeds were less than 4 m s^{-1}, near-surface ε increased with heating and was higher than would be expected based on wind speed alone. Enhancement was moderated by reduced efficiency of mixing. k averaged 10 cm hr^{-1}, ~5 times higher than computed from wind-based models. The equations, which include wind, heating, and mixing efficiency, will enable improved estimates of fluxes of CO_2 and CH_4 used in biogeochemical models of oceans and inland waters during heating and will be especially important in tropical water bodies with high concentrations of climate forcing trace gases.

1. Introduction

Turbulence near the air-water interface in inland waters and oceans mediates the exchange of sparingly soluble gases with the atmosphere for wind speeds up to about 10 m s^{-1} (Brumer et al., 2017; Lamont & Scott, 1970; MacIntyre et al., 2010; Zappa et al., 2007). Turbulence in the upper mixed layer as a whole is of interest as it moderates the amount of heat from the atmosphere that is transferred to deeper depths as needed for climate models (Hughes et al., 2020b; Soloviev et al., 2001). Similarly, it moderates the light exposure of phytoplankton and their nutrient supply. Consequently, the cycles of diurnal stratification and mixing in the upper mixed layer of oceans (Brainerd & Gregg, 1993; Peters et al., 1988; Soloviev et al., 1988) and of lakes (Imberger, 1985) are of considerable importance. Studies of turbulence in tropical regions have been of particular interest with their light to moderate winds and pronounced heating (Soloviev & Lukas, 2006), and diel studies have shown the influence of nocturnal mixing on concentrations and fluxes of CH_4 (Crill et al., 1988) and of diurnal heating and cooling on elevated gas transfer velocities during light and moderate winds (McGillis et al., 2004; Polsenaere et al., 2013). During light to moderate winds, turbulence measurements just below the air-water interface in lakes (MacIntyre

Software: Sally MacIntyre
Supervision: Sally MacIntyre
Validation: Sally MacIntyre
Visualization: Sally MacIntyre
Writing – original draft: Sally MacIntyre
Writing – review & editing: Sally MacIntyre, J. H. F. Amaral, J. M. Melack

et al., 2019, 2021; Tedford et al., 2014) and oceans are rare (Hughes et al., 2020a; Soloviev et al., 1988; Sutherland et al., 2016). In the absence of breaking surface waves, the perturbations of the boundary layer above and immediately below the air-water interface are expected to be small (Hara & Sullivan, 2014). Near the surface when waves are small, and for depths in the mixed layer below those where breaking surface waves have enhanced turbulence, (Soloviev et al., 2001; Terray et al., 1996), the theory and equations developed to quantify turbulence for stable and unstable atmospheric boundary layers, Monin-Obukhov similarity theory (MOST), can be expected to apply (Monin & Obukhov, 1954).

MOST has successfully predicted turbulence, as the rate of dissipation of turbulent kinetic energy (ε), in stable and unstable atmospheric boundary layers (Grachev et al., 2007, 2013; Wyngaard & Coté, 1971) and in oceanic and lacustrine boundary layers under destabilizing (herein, cooling) conditions (Anis & Moum, 1992; Lombardo & Gregg, 1989; Shay & Gregg, 1986; Tedford et al., 2014). The theory has only been applied in a few studies of oceans or lakes under stabilizing conditions (herein, heating) but points to increased values of ε relative to expected values based on shear stress (Soloviev et al., 2001; Tedford et al., 2014). Further effort is warranted as high resolution instrumentation deployed in the upper several meters of oceans and lakes indicates shear and dissipation rates are elevated (Hughes et al., 2020a, 2020b; Sutherland et al., 2016; Yeates & Imberger, 2004). Diurnal warm layers or the related diurnal thermoclines are ubiquitous in tropical regions and in more northern regions during stratified periods (Ward, 2006; Xenopoulos & Schlinder, 2001). Even when winds are light, the water surface can become rippled and capillary-gravity waves may develop leading to an increase in shear, vorticity, and dissipation rates near the air-water interface (Lexague & Zappa 2021; Tsai et al., 2015; Veron & Melville, 2001). While breaking surface waves, which occur at moderate to high wind speeds, increase near-surface turbulence relative to predictions from shear stress (Terray et al., 1996), the effect of small nonbreaking waves on dissipation rates is uncertain (D'Asaro, 2014). Validation or extension of MOST under heating with light winds would enable improved estimates of dissipation rates as needed to compute gas transfer velocities with the surface renewal model (MacIntyre et al., 2010; Zappa et al., 2007).

1.1. Monin-Obukhov Similarity Theory

MOST provides equations to estimate the rate of dissipation of turbulent kinetic energy near the air-water interface in stable and unstable boundary layers (Lombardo & Gregg, 1989; Tedford et al., 2014; Wyngaard & Coté, 1971). These equations can be applied to the surface layer of lakes and oceans when wind speeds are low to moderate with minimal breaking of surface waves (Terray et al., 1996). The relative influence of shear stress versus buoyancy flux (β, where β^- indicates cooling and β^+ heating) on forcing in the surface layer is quantified using the Monin-Obukhov length scale, $L = u_*^3/\kappa\beta$ in the atmosphere and $L_{MO} = u_{*_w}^3/\kappa\beta$, in the water, where shear stress $t = \rho_a u_*^2 = \rho_w u_{*_w}^2 = \rho_a C_d U^2$ and ρ_a and ρ_w are density in the air and water respectively, C_d is the drag coefficient at instrument height, U is wind speed, κ is the von Karman constant, and u_* and u_{*_w} are the friction velocities in the air and water respectively. Predictive equations for momentum, heat flux, and dissipation rate are based on the ratio of measurement height to the Monin-Obukhov length scale, that is z/L with the ratio known as ζ (Monin & Obukhov, 1954). In the water column, the ratio is z/L_{MO}. The nondimensional vertical gradient of mean wind speed, U, is expressed as $\varphi_m(\zeta) = (\kappa z/u_*) \cdot$ dU/dz where z is instrument height and dU/dz is the velocity gradient. During stable conditions, the velocity gradient is intensified whereas under unstable conditions it is diminished relative to neutral conditions (Csanady, 2001). The nondimensional velocity gradient in the near-surface of lakes and oceans similarly can be expressed as $\varphi_m(\zeta) = (\kappa z/u_{*_w})\, du/dz$ with u velocity. Hence, as in the atmosphere, during heating as the surface boundary layer becomes stably stratified, shear is increased (Csanady, 2001; Soloviev & Lukas, 2006; Thorpe, 2007).

Dissipation rates also depend on ζ. For neutral stratification in the upper water column with light to moderate winds, $\varepsilon = u_{*_w}^3/\kappa z$. This relation is known as law of the wall scaling, and we let ε_s be dissipation rate so predicted. Taking into account the effects of buoyancy flux, $\varepsilon = \varepsilon_s \varphi_\varepsilon$, and φ_ε typically has the form $\varphi_\varepsilon = A_A + B_A |\zeta|$ with A_A and B_A empirically derived coefficients. When obtained under destabilizing conditions, the coefficients have been found to be similar in near-surface boundary layers in the atmosphere (Wyngaard & Coté, 1971), ocean (Anis & Moum, 1992; Lombardo & Gregg, 1989; Shay & Gregg, 1986), and lakes (Jonas et al., 2003; Tedford et al., 2014). A_A is ~1 and B_A is less than 1 (Lombardo & Gregg, 1989; Tedford et al., 2014; Wyngaard & Coté, 1971). Under stabilizing conditions in the atmosphere, diverse observations indicate $A_A = 1$ and $B_A = 5$ (Grachev et al., 2007, 2013, 2015) although formulations have been expressed in more complex and in more

simplified ways (Sanz Rodrigo & Anderson, 2013; Tedford et al., 2014; Wyngaard & Coté, 1971). For the conditions included in our study, destabilizing conditions occurred when the water surface cooled, and stabilizing conditions occurred when it was heating. Under heating, the shear stress in the surface layer is increased for a given wind speed relative to neutral conditions (Csanady, 2001). Under cooling in lakes and oceans, the development of instabilities and resultant thermals, reduces near-surface shear (Bouffard & Wuest, 2019; Tedford et al., 2014). The larger multiplier on ζ under heating than cooling captures these differences and implies that when winds are light the increase in dissipation rates will be greater under heating than cooling. Thus, via MOST, increased near-surface shear and associated increased near-surface dissipation rates can be quantified as the stability of surface waters varies.

The ongoing efforts to quantity the empirical coefficients for MOST under stable stratification in the surface layer of the atmosphere are based on the turbulent kinetic energy budget (Grachev et al., 2015; Sanz Rodrigo & Anderson, 2013). The turbulent kinetic energy budget where e is TKE and t is time is $d<e>/dt + P + b + T + \varepsilon = 0$. That is, the change in TKE over time depends on production (P, also called m by convention), buoyancy flux (b) within the layer, vertical transport (T) of TKE including pressure fluctuations, and dissipation (Endoh et al., 2014; Grachev et al., 2015; Osborn, 1980; Turner, 1973). Under heating, the budget is assumed steady and the vertical transport terms have been shown to be small (Grachev et al., 2015). The term b is generally thought of as mixing, the interleaving of packets of denser water from below with lighter water above creating water of intermediate density. That is, $b = g/\rho <\rho' w'>$ where g is gravity, ρ is density, and w is vertical velocity and primes indicate fluctuations from the mean (Osborn, 1980). The production of turbulence by shear ($m = <u'w'>dU/dz$) is then balanced by the conversion of kinetic energy to irreversible potential energy (b) and dissipation. Although the sign conventions have varied in the budgets (Gregg et al., 2018; Osborn, 1980), for the case of heating and evaluation of the flux Richardson number to follow, all terms are positive: $m = b + \varepsilon$ (Ivey & Imberger, 1991; Osborn, 1980).

The flux Richardson number (R_f) is the ratio of buoyancy flux to turbulence production (Gregg et al., 2018) and is written as $R_f = b/m$ which is $b/(b + \varepsilon)$ at steady state (Ivey & Imberger, 1991). Importantly, when values of R_f are close to critical values, ~0.2 in atmospheric studies and 0.17 in oceanographic ones, calculated values of R_f are similar regardless of whether the denominator does or does not include the nonsteady and transport terms (Venayagamoorthy & Koseff, 2016). Hence, $m = b + \varepsilon$ applies for $R_f < \sim 0.2$. In the framework of MOST, the expression is written as $\varphi_m (1–R_f) = \varphi_\varepsilon$ where φ_m is the nondimensional velocity gradient near the surface and the nondimensional shear-production of turbulence (Grachev et al., 2013, 2015). Because R_f is small, and assuming A_A is 1, the expressions for φ_m and φ_ε are similar: $\varphi_a = 1 + B_A \cdot \zeta$ where a can be m or ε and B_A has a value of 5 when R_f is at its critical value of 0.2 (Grachev et al., 2013). $B_A = 5$, as found in the atmospheric studies, is equivalent to $1/R_{fcrit}$ (Grachev et al., 2013). Smaller values of B_A occur when stratification is stronger and damps the turbulence such that R_f exceeds critical values (Grachev et al., 2013). It is not known how B_A varies when R_f is below critical values.

The continued introduction of energy from the wind into near surface waters may lead to an intensification of shear and continuous formation of instabilities such that R_f is less than critical and B_A is larger than in atmospheric studies during heating. The high values of near-surface shear and dissipation in Sutherland et al. (2016) and Hughes et al. (2020a, 2020b) in the diurnal warm layer support that hypothesis, as does the decrease in the gradient Richardson number, $Ri_g = g/\rho\ (d\rho/dz/(du/dz)^2$, from ~0.001 to 0.2 from the near-surface to the base of the mixed layer (Yeates & Imberger, 2004). For Ri_g less than the critical value of 0.25, R_f and Ri_g co-vary (Venayagamoorthy & Koseff, 2016). Values below critical are particularly likely in diurnal thermoclines and wind-driven mixed layers (Imberger & Ivey, 1991). Such occurs when dissipation rates exceed the available potential energy in instabilities, the turbulence is classified as energetic, isotropic, and growing, and the mixing efficiency, variously called R_f or $R_f/(1\text{-}R_f)$, is low (Ivey & Imberger, 1991; Monismith et al., 2018; Shih et al., 2005). R_f decreases as instabilities form (Smyth et al., 2019). For variable R_f below the air-water interface, instantaneous values of B_A may vary as $1/R_f$. The mean value of B_A may have a higher value near the surface than at deeper depths in the mixed layer. Thus, we hypothesize that the increases in ε beyond that expected from wind induced shear under heating will be moderated by $B_A\zeta$ with the mean value of B_A near the surface higher than in atmospheric studies and in the water below.

R_f and the extent of isotropy can be determined from the buoyancy Reynolds number, $Re_\beta = \varepsilon/\nu N^2$. $(Re_\beta)^{1/2}$ is defined as the ratio of the rate of strain of the small-scale fluctuations, γ, where $\varepsilon = \nu\, \gamma^2$, to the buoyancy frequency

($N = (g/\rho\ d\rho/dz)^{1/2}$ where g is gravity, ρ is density, and z is depth) (Ivey & Imberger, 1991). $Re_\beta = (L_o/L_k)^{4/3}$, the ratio of the Ozmidov length scale (L_o) to the Kolmogoroff length scale (L_K). $L_o = (\varepsilon/N^3)^{½}$, the largest eddy size not influenced by stratification, and $L_K = (\nu^3/\varepsilon)^{1/4}$ and considered the smallest eddy size in a turbulent flow (Tennekes & Lumley, 1972). Once Re_β exceeds 200, the turbulent flow is considered isotropic (Gargett et al., 1984). Experimental and modeling studies have illustrated that as Re_β progressively increases above a threshold, often ~100 but in some experiments over 1,000, R_f decreases (Kirkpatrick et al., 2019; Monismith et al., 2018; Shih et al., 2005). The expected decrease in R_f with Re_β has been found in stratified near-shore flows and near boundaries where the ratio of $L_o/\kappa z > 0.25$ (Holleman et al. 2016; Monismith et al., 2018) although not necessarily in offshore waters away from boundaries (Ivey et al., 2018; Monismith et al., 2018). With respect to near-surface waters under light winds and heating, we predict that Re_β will exceed 200 which implies that the energy being dissipated will exceed that required for mixing. Thus, we predict ζ and R_f together will determine φ_ε.

Further variability in φ_ε may be induced if surface waves form. An additional velocity term, Stokes drift, develops due to the overall forward motion of the oscillatory motions from the surface waves. Shear production is modified by inclusion of Stokes drift and is included in the term m, described above (Sjöblom & Smedman, 2002). When swell is present in atmospheric studies, it contributes to vertical flux of momentum via pressure fluctuations and is included in the transport term of the TKE budget. As a result of the interaction of Stokes drift and shear driven currents, Langmuir cells can form once winds exceed 3 m s^{-1} (Leibovich, 1983). At their onset, they can be of order 4–10 cm in width and lead to increases in ε (D'Asaro, 2014; Veron & Melville, 2001). Small amplitude surface waves can form without formation of Langmuir cells and augment existing near-surface turbulence and mixing (Dai et al., 2010; Tsai et al., 2015, 2017). That said, increases in Stokes drift and the related shear may be constrained to depths of a few centimeters (Laxague & Zappa, 2020. Micro-wave breaking, which is known to increase surface divergence and gas transfer velocities, becomes important at moderate wind speeds (Turney & Banerjee, 2013.) Near-surface shear can also be moderated by high frequency waves near the surface (Moum et al., 2003; Soloviev & Lukas, 2006; St. Laurent & Merrifield, 2017). Variability in φ_ε may also result from unsteady winds.

1.2. The Surface Renewal Model

The surface renewal model used to calculate gas transfer velocities incorporates ε. Thus, comparisons of measured fluxes with those calculated using the surface renewal model provide a mechanism to determine the accuracy of computing ε following MOST. The surface renewal model, $k = c_1(\varepsilon\nu)^{1/4}Sc^{-n}$, explicitly incorporates turbulence as ε (MacIntyre et al., 1995; Zappa et al., 2007). ν is kinematic viscosity, c_1 is a coefficient theoretically shown to be ~0.4 (Katul et al., 2018), Sc is the Schmidt number, and n is 2/3 for solid surfaces and ½ for fluid ones (Jähne et al., 1987). Estimates of fluxes obtained using the small-eddy version of the surface renewal model and ε modeled using MOST are proving to be accurate at low to moderate wind speeds when compared with direct observations of fluxes using eddy covariance systems (Czikowsky et al., 2018; Heiskanen et al., 2014; Mammarella et al., 2015) or chambers (MacIntyre et al., 2021). These results point toward successful modeling of dissipation rates using MOST. The equivalence of fluxes from the two approaches implies that the physical processes incorporated in MOST predominate under light to moderate winds. However, these and other studies have not evaluated MOST during conditions of heating and light to moderate winds. This effort requires comparisons of estimates of k from measurements of fluxes and concentrations with estimates of k obtained with the surface renewal model when ε is obtained from physical instrumentation such as microstructure profilers and when ε is calculated from time series measurements of temperature and meteorology using MOST. Doing so is a major goal of our study.

1.3. Goals and Location of the Study

Tropical lakes provide an excellent venue to evaluate the implications of near-surface heating on dissipation rates. With strong solar radiation and often weak winds, stratification can form quickly and persist for several hours each day (Augusto-Silva et al., 2019; MacIntyre et al., 2002, 2014). Tropical lakes can have high concentrations of dissolved CO_2 and CH_4 and make a large contribution to regional and global carbon dioxide and methane fluxes (Melack et al., 2004; Raymond et al., 2013; Richey et al., 2002). McGillis et al.'s (2004) observing enhanced CO_2 fluxes during moderate winds and heating in the tropical ocean provides further motivation for focusing on a tropical water body.

The goals of our study are to describe the stratification and to quantify dissipation rates in a tropical water body under light winds, to evaluate how φ_ε varies with ζ just below the air-water interface (e.g., the upper 0.25 m) and in the mixing layer below, and to develop appropriate modifications for the similarity scaling for ε which can be used to compute gas transfer velocities. Measurements include time series meteorology and within lake temperatures which allow calculation of surface energy budgets, stratification within the water column, and changes in depth of the surface layer, also known as the actively mixing layer (z_{AML}). We use temperature-gradient microstructure data to quantify dissipation rates within the upper water column in bins ~0.25 m in vertical dimension. We quantify the extent to which near-surface turbulence is larger under heating or cooling. We further contrast measured near-surface dissipation rates with values computed from the similarity scaling for boundary layers in the atmosphere and in the surface layer of lakes and oceans. We find that increases in ε under light winds and heating follow predictions from MOST, illustrate the larger enhancement due to heating (φ_ε) in the upper 0.25 m than observed in prior atmospheric studies, find the enhancement in the mixed layer below 0.25 m is similar to that in atmospheric boundary layers, extend the range of ζ from prior oceanographic studies, and verify our predicted values of gas transfer velocities with those obtained from chamber measurements. Based on our observations of the water surface, we evaluate whether surface waves contribute to the variability in dissipation rates. With these results, we illustrate near-surface dissipation rates are an order of magnitude higher under heating with light winds than cooling under light winds, that gas transfer velocities under light winds and heating are 2–5 times higher than when computed using wind-based models, and we extend MOST with updated coefficients for φ_ε that take into account the low and variable flux Richardson numbers.

2. Methods

2.1. Site Description

Data were collected in an open water area at the southern end Balbina Reservoir (Brazil) (01°54'38.5" S; 59°28'08.5" W) (Kemenes et al., 2011) from July 14 (DOY 195) to July 20 (DOY 201) 2013. Our primary measurement site was ~300 m from the nearest land. This dendritic reservoir is forested on its shores.

2.2. Field Methods and Calculations

2.2.1. Meteorology, Temperature Arrays and Irradiance

Wind speed and direction, air temperature, and relative humidity were measured on a floating platform at an offshore site (01°54'38.5" S; 59°28'08.5" W) with additional radiation measurements at an inshore site (1° 54' 33.3" S; 59° 27'42.21S W) (MacIntyre, 2021a). Downwelling shortwave radiation was measured with newly calibrated sensors at the offshore site. A net radiometer (Kipp and Zonen CNR1) measured downwelling and upwelling shortwave and long wave radiation at the inshore site. Upwelling shortwave radiation at the offshore site was computed as albedo times downwelling shortwave with albedo calculated taking into account latitude, day of year, time of day, and angle of refraction. Upwelling and downwelling longwave data were corrected for temperature in post-processing based on the mean of the temperature measured by the upwelling and downwelling sensors. The diffuse attenuation coefficient (k_d) was computed following Beer's Law from irradiance measurements from 400 to 700 nm obtained with a 2 π quantum sensor (LI-COR, INC. LI-192). The value was 0.5 m^{-1}.

Time series temperature measurements were obtained from temperature arrays, consisting of newly calibrated, fast-response temperature sensors (RBR Solos with accuracy of 0.002°C and resolution 0.0002°C) sampling at 10 s intervals, and positioned in the upper 20 m offshore (01°54'33.3" S; 59°28'10.7" W) (MacIntyre, 2021b). The array consisted of a taut-line mooring with an upper line from the subsurface buoy to a thin float on the water surface. One sensor was attached horizontally to the base of the float, which shielded it from direct solar radiation, allowing temperature measurements at ~0.05 m. Two other loggers, facing downwards, were suspended from the float and obtained measurements at 0.5 and 0.95 m. The remaining loggers were below the subsurface buoy and measured temperatures at 1.15 and 1.75 m and every 1.5 m thereafter.

2.2.2. Microstructure Data and Analysis

Temperature-gradient microstructure profiles were obtained with the self-contained autonomous microstructure profiler (SCAMP) (MacIntyre, 2021c) with details on the instrument and data analysis in MacIntyre et al. (1999) and Tedford et al. (2014). Data were obtained in blocks of 6–10 profiles from early morning through late evening.

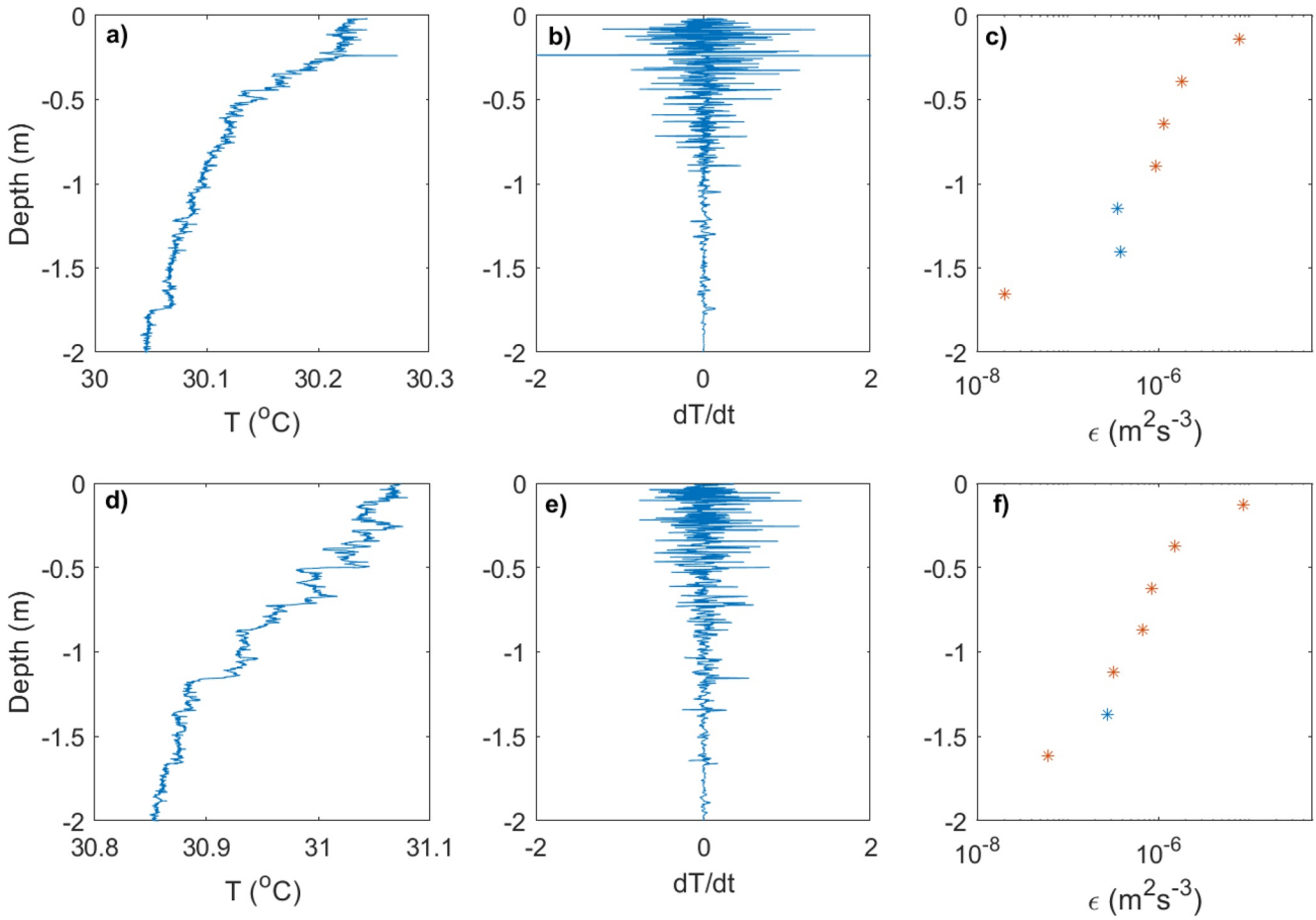

Figure 1. Profiles in the upper 2 m of temperature (T), change of temperature divided by the rising speed of the SCAMP (dT/dt), and dissipation rate (ε) (orange symbols—quality controls met; blue symbols quality controls not met) during morning heating (0947 hr July 17, 2013 (day of year [DOY] 198) (a–c) and late in the heating period (1309 hr July 16, 2013 [DOY 197] (d–f) illustrating that the stably stratified upper water column contains many small instabilities as expected for shear-driven turbulence. The depth of the actively mixing layer, calculated using the time-series temperature data (see below), was 1.3 and 1.75 m for the two times, respectively.

Profiles were taken in upcast mode in the upper 10 m with a rise speed close to 0.1 m s^{-1} and sampling frequency of 100 Hz enabling 1 mm vertical resolution. The instrument is designed such that it descends away from the boat on deployment, drops a weight, and rises away from the boat. The sensor's passing through the air-water interface was identified by temperature rapidly decreasing by 0.05°C; data above that depth were not used.

Analysis included computation of ε, rate of dissipation of turbulent kinetic energy, and χ, the rate of dissipation of temperature variance (Osborn & Cox, 1972), from the temperature-gradient signal in ~0.25 m bins. As in Tedford et al. (2014), ε and χ were obtained by fitting the theoretical temperature-gradient spectrum of Batchelor (1959) to the temperature-gradient spectrum calculated from the SCAMP data. Fitting was done using the maximum likelihood techniques of Ruddick et al. (2000). To avoid contamination with noise when turbulence was weak, spectra were fit over the range of wave numbers from the upper bound of the inertial convective subrange to the intersection of the observed spectrum with the model noise (Steinbuck et al., 2009). This technique was only required for $\varepsilon < 10^{-7}$ m^2 s^{-3}. Dissipation rates were rejected if the logarithm of the likelihood ratio was less than 2, the mean absolute deviation was greater than $2(2/d)^{-1/2}$ where d is 4 degrees of freedom, and the signal-to-noise ratio was less than 1.3 (Ruddick et al., 2000) (Figure 1). The change in potential energy in the water column due to mixing, that is, buoyancy flux, b, was calculated in the upper 0.12 and 0.25 m as $b = 0.5\ (\mathrm{dT/dz})^{-2}\ \chi\ N^2$ (Osborn & Cox, 1972) where dT/dz is the temperature gradient computed from temperature profiles averaged to ~0.02 m intervals and sorted to decrease monotonically. We present results using dT/dz for the upper 0.12 m as Thorpe scales (see below) were predominantly this size or smaller during heating. With the simplification of the

TKE budget as justified in the introduction, production = $b + \varepsilon$ (Ivey & Imberger, 1991; Osborn, 1980). The flux Richardson number (R_f) is indicative of the efficiency of mixing and computed as $R_f = b/(b+\varepsilon)$ (Ivey & Imberger, 1991). Calculations were conducted during the heating period, ~0830 to ~1530 hr, with time intervals for each day carefully identified by inspection of the time-series temperatures.

Thorpe scales and centered displacement scales (L_c) which characterize the size of turbulent eddies, or overturns, in the flow field, were obtained as in Imberger and Boashash (1986). Buoyancy frequency was computed from the density profile after it was sorted to be monotonic. We also computed a number of variables which describe the nature of the turbulence itself. These include the turbulent Froude number $\mathrm{Fr_T} = u/\mathrm{NL_c}$ where L_c is the root mean square (rms) of the largest overturns and u is the rms velocity scale $u = (\varepsilon \cdot L_c)^{1/3}$, and the turbulent Reynolds number $\mathrm{Re_T} = uL_c/\nu$ (Ivey & Imberger, 1991. Fr_T and Re_T, can also be written as ratios of length scales in the flow, with $Fr_T = (L_o/L_c)^{2/3}$ and $Re_T = (L_c/L_K)^{4/3}$ where the Ozmidov length scale, L_o, and the Kolmogoroff length scale, L_K, were defined previously. The buoyancy Reynolds number, Re_β, described in the introduction, indicates whether the turbulent flow is anisotropic or isotropic as do Thorpe scales or rms centered displacement scales less than L_o and $Fr_T > 1.5$. R_f is expected to be below critical values when $Fr_T > \sim 1.5$ (Ivey & Imberger, 1991).

2.2.3. Methane Concentrations and Fluxes

Methane concentrations were obtained using the headspace method with sample volumes for water and headspace both 30 mL (Hamilton et al., 1995). The equilibrated air was transferred to 25 mL glass vials which had been acid washed and rinsed, sealed with thick butyl rubber stoppers, and kept in the dark at room temperature (18°C) until analysis within one month in a gas chromatograph (Thermo Scientific) equipped with a flame ionization detector. Calibrations, using 10 and 100 ppmv standards (Air Liquide, USA) were performed before analysis began and recalibration was done after every 25 to 30 samples. Solubility coefficients were applied to calculate the final methane concentrations (Yamamoto et al., 1976).

Methane fluxes were obtained using floating chambers with an initial sample and subsequent samples every 5 min over 15-min. All air samples taken from the chambers were transferred to glass vials as above until analyzed using the gas chromatograph. Chambers had an internal volume of 15 L, a surface area of 0.11 m^2, and extended 0.06 m below the water surface. Only results in which the r^2 value exceeded 0.85 were used. Barbosa et al. (2016) provide additional methodological details. Ebullition detected by rapid changes in concentration was noted only once; ebullition is a minor flux in Balbina Reservoir (Kemenes, 2006). Gas transfer velocities were obtained as $k = F/(C_w - C_{eq})$, where F is flux, C_w is the concentration of CH_4 in surface water, and C_{eq} is the concentration in equilibrium with the atmosphere at the top of the aqueous boundary layer. Values of k were normalized to k_{600}, equivalent to that for CO_2 in freshwater at 20°C, where Schmidt numbers as a function of temperature were computed following Wanninkhof (2014).

2.2.4. Calculations With Time-Series Data

The shear stress on the water surface is calculated as $\tau = \rho_a C_d U^2$ where ρ_a is density of the air, C_d is the drag coefficient at instrument height taking into account atmospheric stability, and U is wind speed at instrument height. Shear stress is defined as $\tau = \rho_a u_*^2$ where u_* is the friction velocity. The expression for shear stress on the water side of the air-water interface is; $\tau = \rho_w u_{*_w}^2$ with ρ_w the density of water and u_{*_w} the water friction velocity. The calculation for C_d uses the Hick's interaction loop and takes into account atmospheric stability (Hicks, 1975). Details of these calculations are in MacIntyre et al. (2002, 2014, 2021) and comparisons with u_* obtained using eddy covariance indicate values are within 10% of those expected from the COARE equations at light to moderate winds (Fairall et al., 1996; Tedford et al., 2014).

Latent and sensible heat fluxes, surface heat flux, net heat flux into the actively mixing layer, buoyancy flux (β) into the reservoir and buoyancy flux (β_*) into the actively mixing layer, Monin-Obukhov length scale in the atmosphere (L) and in the water (L_{MO}), water friction velocity (u_{*_w}); velocity of thermals from heat loss (w_*), buoyancy frequency (N), and wind speed at 10 m height (U_{10}) were calculated as in MacIntyre et al. (2002, 2014, 2021). The surface energy budget and wind speed-related calculations take into account the stability of the atmosphere above the water surface, and previous comparisons indicate that momentum and sensible and latent heat fluxes are within 10% of results obtained using COARE equations (Fairall et al., 1996; Tedford et al., 2014). Surface heat flux is the sum of latent and sensible heat fluxes and net long wave radiation. The total heat flux (H, W m^{-2}) is the sum of incoming short wave radiation and the surface heat fluxes, and net heat flux, also called effective heat flux (H_*), is the sum of the surface heat flux and net short wave radiation retained in the actively mixing layer

(Imberger, 1985). Penetration of short wave radiation was calculated as described in Jellison and Melack (1993) with the attenuation from 400 to 700 nm computed from profiles of underwater irradiance as described above. Surface buoyancy flux (β, $m^2\ s^{-3}$) is calculated from total heat flux as: $\beta = g\alpha H/(C_{pw}\rho_o)$ where g is gravity, α is the thermal coefficient of expansion, C_{pw} is specific heat capacity, and ρ_o is density of water at the surface. Buoyancy flux into the actively mixing layer, β_*, is similarly calculated with H_* instead of H. L_{MO} is calculated using β_*, that is $L_{MO} = {u_{*_w}}^3/\kappa\beta_*$.

The depth of the actively mixing layer (z_{AML}) was computed as the first depth below the surface where temperatures were within 0.005°C of surface temperatures during cooling and, for part of the heating period, as the first depth where the increase in density exceeded 0.1 kg m^{-3} relative to the near-surface value. The first criterion is based on recognizing that under convection near-surface temperatures are generally slightly cooler than the water immediately below and mixing will occur to the stably stratified water below (Anis & Moum, 1992; Shay & Gregg, 1986). The second criterion recognizes that when the water column is stratified near the surface, mixing can extend into the stratified layer (Brainerd & Gregg, 1995). We determined these criteria based on examination of the 10 second time-series temperature data, density gradients, and microstructure data. We used the temperature criterion beginning mid-afternoon when the reservoir began to lose heat until early the following morning when it began to gain heat. Two additional criteria were required to ensure that estimated z_{AML} followed the patterns evident in the microstructure profiles and the time-series temperature data. Due to penetrative convection continuing for a short period after sunrise and resulting entrainment of cooler water, incoming short wave radiation began to increase prior to the upper water column's beginning to gain heat. Thus, we set a fixed depth for z_{AML} at that time in order to assure that heat flux remained negative. As the lake initially began to gain heat, the temperature criterion underestimated the depth of the actively mixing layer and the density criteria overestimated it. For that nearly 2-hr period, the near-surface gradients in density continuously increased. Hence, we fixed z_{AML} as 1.3 m based on examination of the many profiles of dissipation rate during that period and by verifying the sign of the resultant heat fluxes into the actively mixing layer relative to increases and decreases in temperature in the upper 2 m. Figures 1a–1c illustrate data obtained during the early morning period in which we applied the fixed depth criteria. Figures 1d–1f illustrate data obtained during the later period of heating when we applied the density criteria. The depth to which dissipation rates were measurable did vary between individual casts during early morning such that some error occurred in the calculation of heat flux and buoyancy flux in the actively mixing layer. These, in turn, influenced the sign and magnitude of the calculated L_{MO}. However, as shown below, the changes in near-surface turbulence predominantly correspond to predictions based on these terms.

The turbulent Langmuir number, was calculated following McWilliams et al. (1997) as $La_T = (u_{*_w}/U_S)^{1/2}$, where Stokes drift is estimated as $U_S = 0.11u_*$ (Csanady, 2001). For the shear stress in this study, drift ranges from 0.002 to 0.016 m s^{-1}. Our estimates are supported by wave measurements in fetch limited situations in which U_S ranged from 0.004 to 0.014 m s^{-1} for wind speeds of 4 m s^{-1} (Lien et al., 2008).

The rate of dissipation of turbulent kinetic energy was computed with the time series meteorological and temperature data using the similarity scaling in Tedford et al. (2014) and in Wyngaard and Coté (1971) under cooling and heating. Under heating, we additionally computed ε using the similarity scaling in Grachev et al. (2013) and Sanz Rodrigo and Anderson (2013). Based on our earlier hypothesis, we also computed $\varepsilon = \varepsilon_s\ (1 + B_A\ |\zeta|)$ letting B_A equal $1/R_f$. We used two approaches for this calculation. In the first, we computed R_f as $2 \cdot Re_\beta^{-0.55}$ where $Re_\beta = \varepsilon/\nu N^2$ (Monismith et al., 2018). In this approximation, we computed Re_β using an initial estimate of ε obtained following Grachev et al. (2013). In this calculation, R_f varies over time. We also calculated the arithmetic mean value of R_f, R_{fmean}, from the microstructure data as described above during the heating period. We then calculated $\varepsilon = \varepsilon_s\ (1 + 1/R_{fmean} \cdot |\zeta|)$.

We obtained φ_ε for the microstructure results by dividing the dissipation rates from the SCAMP with those expected on the basis of shear under a neutral atmosphere, ε_s. That is, $\varphi_\varepsilon = \varepsilon\kappa z/{u_{*_w}}^3 = \varepsilon/\varepsilon_s$. For these calculations, we let $z = 0.15$ as it is approximately the midpoint of the upper bin used to calculate dissipation rates with the temperature-gradient microstructure data. Choosing this depth allowed us to compare φ_ε versus ζ for the SCAMP data with φ_ε from the various models.

2.2.5. Calculations of Gas Transfer Velocities

The gas transfer velocity normalized to that for CO_2 at 20°C, k_{600}, was computed using the small eddy parameterization of the surface renewal model using ε calculated from microstructure data and ε obtained from similarity

scaling: $k_{600} = c_1(\varepsilon\upsilon)^{1/4}Sc^{-1/2}$ where Sc is the Schmidt number for CO_2 at 20°C, 600 (MacIntyre et al., 2010; Zappa et al., 2007). Zappa et al. (2007) found the coefficient c_1 to average 0.419, Katul et al. (2018) determine on theoretical grounds that it will be ~0.4, and Wang et al. (2015), who present their own results and review those of others, found the coefficient to increase for ε above 10^{-6} m^2 s^{-3}. Given that the upper bound for dissipation estimates with the SCAMP is ~10^{-5} m^2 s^{-3}, and the relative invariance of the coefficient in Wang et al. (2015) for typical dissipation values in the upper mixed layer of lakes, we assume the coefficient is a constant, and given the uncertainty, use the value 0.5 as in MacIntyre et al. (1995, 2019, 2021).

2.2.6. Calculation of the Coefficient of Eddy Diffusivity With Microstructure Data

During heating when turbulence was induced by shear, we computed the coefficient of eddy diffusivity (K_z) following Osborn (1980) with the modifications in Shih et al. (2005) and Bouffard and Boegman (2013). That is, $K_z = \Gamma\ \varepsilon N^{-2}$ in which the mixing efficiency $G = R_f/(1\text{-}R_f)$.

Under cooling, we compute K_z as b/N^2 (Wuest & Lorke, 2003) and incorporate its depth dependence by assuming $b = \beta$ [1–1.1(z/H)] where z is depth, H is the depth of the actively mixing layer, z_{AML}, and β is surface buoyancy flux (Chou et al., 1986; Imberger, 1985). By applying Osborn's (1980) model, $K_z = \Gamma\ \varepsilon/N^2$ and, as in Chou et al. (1986), dissipation rate a constant fraction of β through the actively mixing layer, and let the variable η be the inverse of the fraction of β which dissipates, $K_z = \eta$[1–1.1(z/H)] ε/N^2. The analysis leads to $b = \Gamma\varepsilon$. Dissipation rates during cooling are often in the range of 0.4–0.8 β (Tedford et al., 2014). Under cooling K_z is only meaningful in the actively mixing layer where temperature decreases with depth, and given the typical curvature of temperature profiles under convection (Anis & Moum, 1995; Shay & Gregg, 1986), is often the mid-point of the mixing layer. Thus, at a depth 0.6H, $K_z = 0.4\ \varepsilon N^{-2}$ for $\varepsilon = 0.8\ \beta_o$, and $K_z = 0.9\ \varepsilon N^{-2}$ for $\varepsilon = 0.4\ \beta_o$. We assume an intermediate value and estimate K_z as $K_z = 0.7\ \varepsilon N^{-2}$ with the additional caveats that the estimates only apply at depths below which temperature decreases in the actively mixing layer and, as is evident in the microstructure data shown below, ε is not a fixed fraction of β in individual microstructure casts.

3. Results

In the following, we first describe the observational data including meteorology, thermal structure, the surface energy budget, and the microstructure data. Subsequently, we highlight aspects of the microstructure results which set the observations apart from those in other studies. These include relatively high values of ε, that is, $>10^{-6}$ m^2 s^{-3} and up to the maximum that can be quantified with the SCAMP, ~2×10^{-5} m^2 s^{-3} for light winds and buoyancy frequency in the water column between 10 cycles per hour (cph) and 25 cph, higher than in many of the recent studies illustrating similarly high dissipation rates in the diurnal warm layer. We provide a diagram illustrating the accentuation of ε relative to values expected from law of the wall scaling (φ_ε) for $0.01 < z/L_{MO} < 100$ and illustrate the more extended range compared with oceanographic studies. We illustrate the greater accentuation relative to models developed for stable stratification in atmospheric boundary layers and in the surface layer of lakes. We also include comparison of gas transfer coefficients obtained with chambers on the water surface and those obtained using the surface renewal model calculated using values of ε with the SCAMP data and the modeled data, including the model we updated by using variable values of R_f to obtain ε.

3.1. Meteorology and Thermal Structure

Meteorological forcing at Balbina Reservoir included strong solar radiation with peaks in the day of 900 W m^{-2}, warm air temperatures, and light winds (Figure 2). These conditions led to temperatures in the upper meter increasing by 1°C–2°C by mid-afternoon and were conducive to generating strong stratification in the upper 2 m and diurnal thermoclines which initially extended to the air-water interface (Figures 1–3). With surface water temperatures of ~30°C even at night, typically warmer than air temperatures, and continued light winds during day and night, the atmosphere was always neutrally stratified or unstable, and latent heat fluxes were appreciable. Surface heat fluxes, beginning by late afternoon and continuing through the night, were between −100 and −300 W m^{-2} and led to erosion of the stratification which had formed in the day (Figures 2 and 3).

Shifts in wind direction coincided with conditions leading to heating and cooling within the upper water column (Figures 2 and 3). Winds were westerly from mid-morning until afternoon. During this time, air temperatures rose, relative humidity decreased, and winds increased from early morning lulls up to 3 or 4 m s^{-1}. Total heat

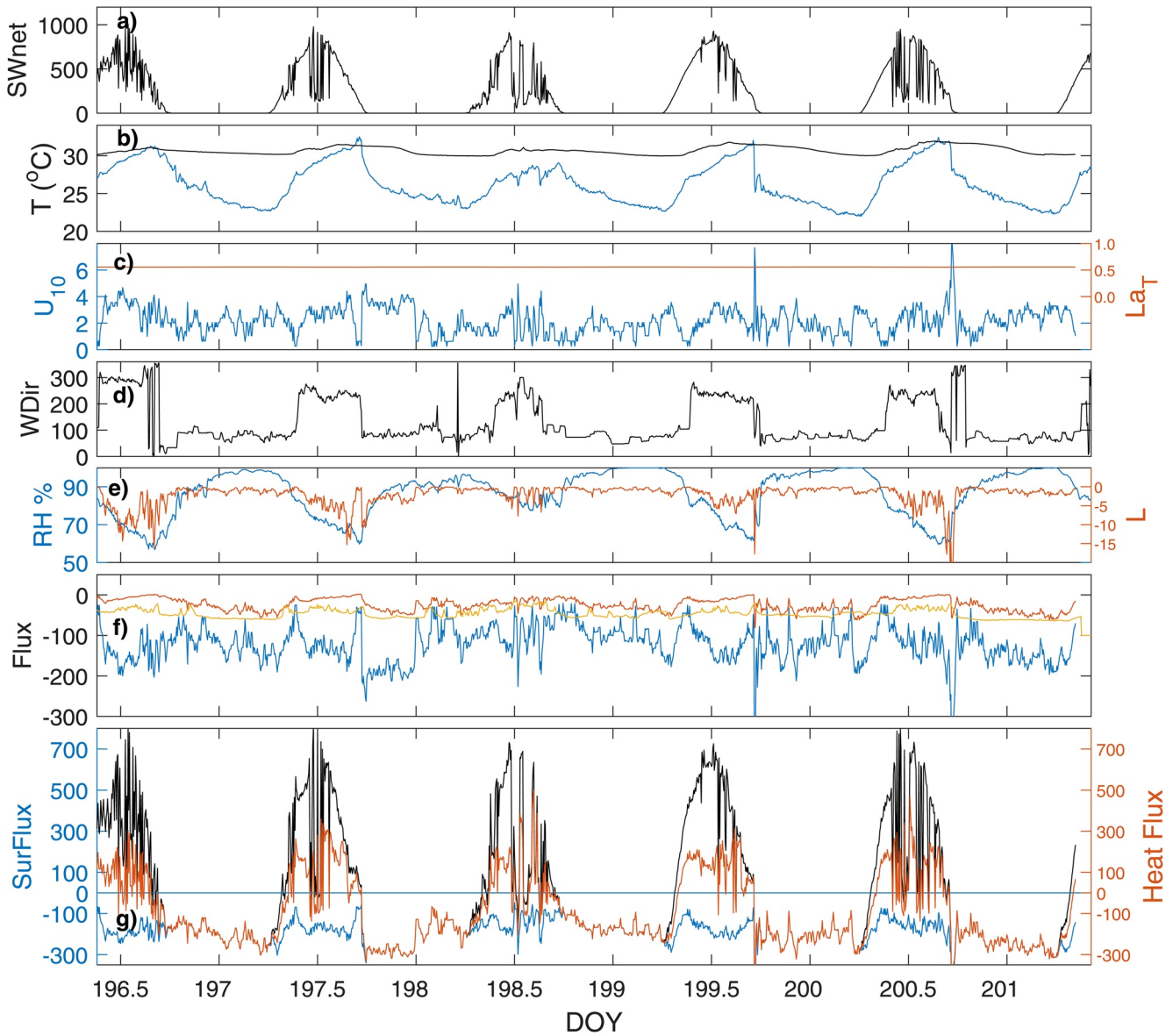

Figure 2. (a) Net short wave radiation (SWnet, W m^{-2}), (b) Air (blue) and surface water temperature (black) (T), (c) U_{10} (wind speed in m s^{-1}corrected to 10 m height taking into account atmospheric stability) (blue) and turbulent Langmuir number La_T (red); (d) Wind direction (WDir, degrees, black), (e) Relative humidity (RH, blue) and Monin-Obukhov length scale (L, red), (f) Latent (blue), sensible (red), and net long wave radiation (yellow) (Flux, W m^{-2}), (g). Surface (SurFlux, blue), total (black) and effective heat fluxes (red) in W m^{-2} in Balbina Reservoir for DOYs 196–201, 2013. Panels (f and g) were ranged to show typical fluctuations, not those during squalls. During squalls, latent heat and surface fluxes reached −550 and –650 W m^{-2}, respectively.

fluxes and effective heat fluxes (H_*), that is, the sum of surface heat fluxes and incoming radiation within the actively mixing layer, rose abruptly during the lull in wind speeds typical shortly after dawn (Figure 2g). Maximal values during the early morning heating period ranged from 400 to 600 W m^{-2} and 100–200 W m^{-2}, respectively. The increase led initially to stratification in the upper 0.5 m and eventually the upper 2 m (Figures 1 and 3d) with buoyancy frequencies in the upper 0.5 m increasing to maxima of 10 or 30 cph with variability dependent on onset and magnitude of winds (Figure 3e). Due to the intermittent high cloud cover, H_* often decreased and became negative in the day causing intermittent cooling of the upper water column. Although total heat fluxes often reached 700 W m^{-2}, with the increases in wind speed and related increase in latent heat flux, H* only occasionally increased above the mid-morning maxima, stratification weakened in the upper 0.5 m with the associated mixing, and stratification in the water below increased as the diurnal thermocline descended. Often the descents were abrupt, particularly if they were associated with subtle changes in wind direction. Mid-to late afternoon,

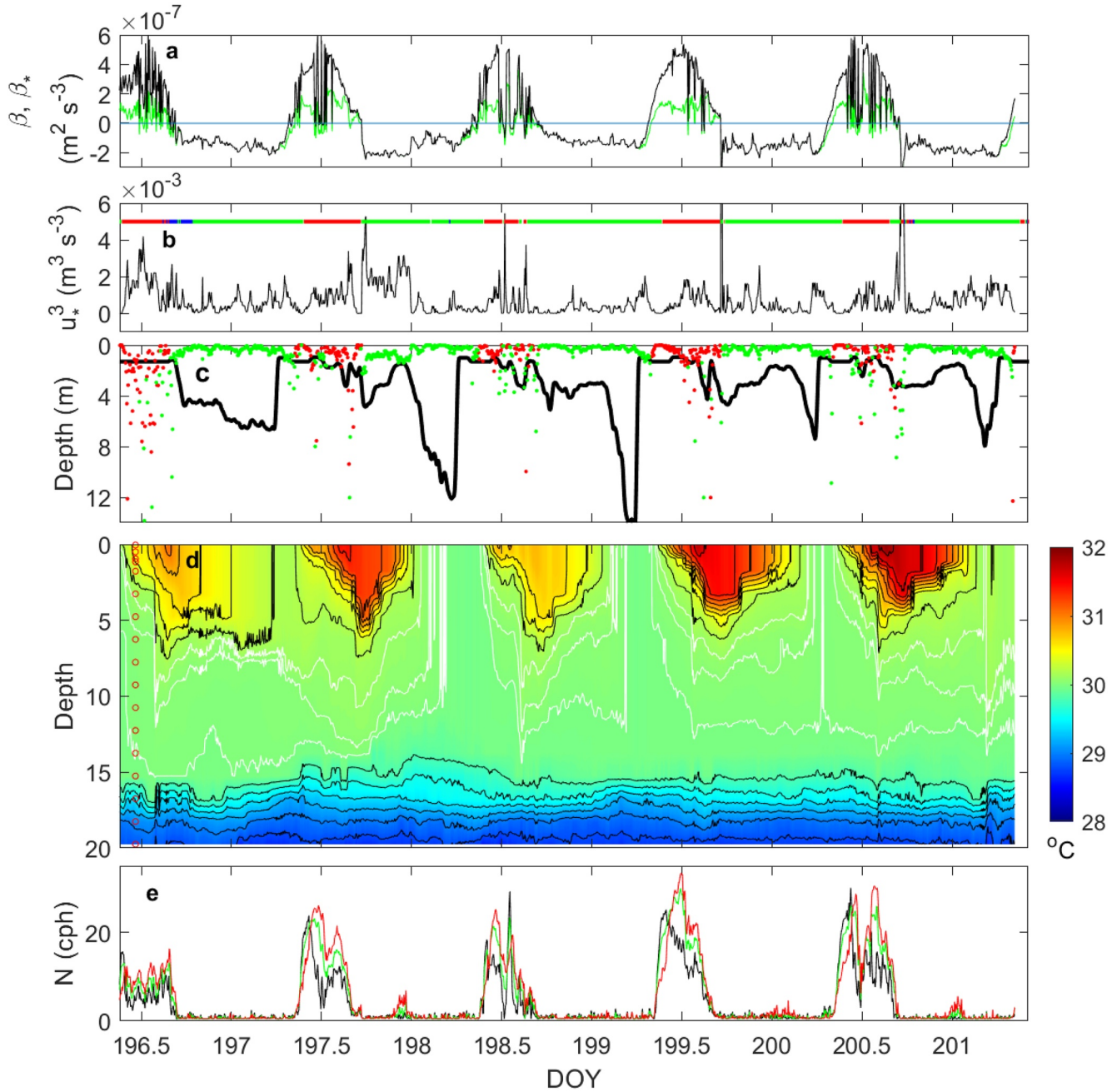

Figure 3. (a) Buoyancy flux (β) (black) and buoyancy flux in the actively mixing layer (β_*) (green); (b) Friction velocity cubed (u_*^3) with overbars indicating wind direction with west (red) generally coinciding with heating, east (green) generally coinciding with cooling, and occasional north (blue) at the transition; (c). Actively mixing layer depth (black), Monin-Obukhov length scale (L_{MO}) in the water under heating (red) and cooling (green); (d). Temperature contours overlaid with 5 min averaged 0.2°C isotherms (black) and 0.05°C isotherms in the subsurface layer (white), Red circles indicate depths of thermistors; (e). Buoyancy frequency (N) in cycles per hour (cph) for the depth intervals 0.05–0.5 m (black), 0.5–0.95 m (red), and 0.95–1.15 m (green).

winds shifted to easterly, a change that was often initially accompanied by squalls with wind speeds up to 7 m s^{-1} and occasionally northerly winds and rain. The diurnal thermocline initially downwelled and then upwelled in response to the change in wind direction. The shift in wind direction marked the transition to air flow from the forest onto the lake which persisted through the night. Due to the changing air mass, air temperature dropped, relative humidity increased, and with the exception of DOY 197, wind speeds dropped to values less than 2 m s^{-1}. With declining solar insolation, H_* became negative and the upper water column began to cool. At night, wind speeds again varied from 0.5 to 4 m s^{-1}, air temperatures continued to drop, and relative humidity increased. Just

before dawn, winds increased to values between 2 and 3 m s^{-1}. Winds then tapered and remained low until the mid-to late morning shift to westerly winds.

Diurnal stratification and mixing in the upper water column of Balbina Reservoir are directly linked to buoyancy flux (β), and u_*^3 (Figure 3). In Balbina R., as in observations at many locations with low to moderate winds, a diurnal thermocline develops in the day which separates the actively mixing layer from the subsurface, or remnant layer, where turbulence, generated at night by convection, decays (Brainerd & Gregg, 1993; Sutherland et al., 2016). Once buoyancy fluxes become negative (heat loss), the diurnal thermocline is eroded, and depending on the magnitude of β, the mixing may reach the seasonal thermocline and cause it to deepen. An additional control moderates the movement of the diurnal thermocline in Balbina R. It is the upper manifestation of an internal wave field that extends into the seasonal thermocline (Figure 3d). The connectivity is evident when the winds shift to easterly in the afternoon and the diurnal thermocline upwells as do the isotherms in the subsurface layer. The phase of the internal waves may be set by other factors than wind direction. The onset of downwelling began prior to midnight on DOY 196 whereas on most days it cannot be seen due to convective mixing extending to the seasonal thermocline at night. Discriminating downward movement of isotherms in the early morning from direct solar heating is difficult as light penetrates to 12 m and the changes in temperature in the subsurface layer are small. The extent to which the internal wave motions moderate shear below the air-water interface is unknown.

The dynamics within the actively mixing layer depend on β_* which indicates whether this layer heats or cools (Figure 3a). During early morning in the lull before winds shifted to westerly, β_* often increased to nearly 2×10^{-7} m^{-2} s^{-3}, and, u_*^3, which would drive near-surface mixing, was low (Figures 3a and 3b). Consequently, near-surface waters heated rapidly. The actively mixing layer shoaled from its nighttime maxima, and the diurnal thermoclines which formed typically extended to the surface (Figures 1, 3c, and 3d) Changes in L_{MO} ($L_{MO} = u_{*_w}{}^3/\kappa\,\beta_*$) indicate the relative influence of wind power to buoyancy flux. On most days, L_{MO} was small albeit measurable and less than z_{AML}. $|L_{MO}/z_{AML}| < 1$ implies that turbulence production near the surface was induced by shear and exceeds that from buoyancy flux under cooling. Values equal to 1 indicate that shear dominates turbulence production in the actively mixing layer. On the calmest mornings with L_{MO} approaching zero, strong near-surface stratification developed. On slightly windier mornings, as on DOYs 196 and 198, L_{MO} extended beyond the actively mixing layer indicating more heat was mixed downwards. The differences in cloud cover and the magnitude of L_{MO} relative to z_{AML} led to variability in the buoyancy frequency in the upper meter, with surface values on the windier morning, DOY 196, only 5 cph whereas N exceeded 20 cph on calm mornings with clear skies (Figure 3e). While N tended to increase more rapidly at the surface, values below often exceeded 25 cph by late morning as stratification intensified in the diurnal thermocline.

From mid-morning until afternoon, u_*^3 increased and the diurnal thermocline downwelled, usually with abrupt downwelling when squalls occurred (Figure 3). The extent of heating, near-surface stratification, and the downwelling of the diurnal thermocline from mid-morning through mid-afternoon varied with cloud cover and wind velocity. During this later period, N initially decreased more rapidly in the upper 0.5 m than in the water below. When winds shifted to the east and β_* became negative as cooling began, the diurnal thermocline began to upwell, with more rapid upwelling on windier days (e.g., DOY 197) (Figure 3). As cooling continued, the diurnal thermocline shoaled, with shoaling more rapid on windier nights (e.g., DOY 197). Despite β of -1×10^{-7} to -2×10^{-7} m^2 s^{-3} at night, due to high values of N in the diurnal thermocline, it was often not fully eroded until midnight after which deeper mixing typically occurred (Figures 2 and 3).

The variables influencing near-surface turbulence varied over diel cycles (Figure 4). The water friction velocity (u_{*_w}) was less than 0.005 m s^{-1} except during brief squalls, and the convective velocity scale (w_*) was at least twice u_{*_w} at night and at times exceeded 0.01 m s^{-1}. Due to cloudy conditions, β_* often became negative in the day such that w_* was positive at such times. While measurable u_{*_w} implies wind shear will develop in the upper-most surface layer, the increases in w_* imply that cooling may deepen the actively mixing layer and disrupt shear driven flows. $|\beta_*|$ was less than $u_{*_w}{}^3/\kappa z$ except when winds were low particularly during the morning and at night (Figure 4b). When the terms are plotted as a ratio, $|z/L_{MO}|$, on a logarithmic scale, the times when β_* will contribute to increasing dissipation rates above those expected for neutral stratification become evident (Figure 4c). That is, for $\varphi_\epsilon = \epsilon_s\,(1 + B_A|z/L|)$, φ_ϵ begins to exceed 1 when $|z/L| > 0.1$ (Grachev et al., 2013; Wyngaard & Coté, 1971). It is during morning heating that the contribution of β_* to dissipation rates is likely to be largest.

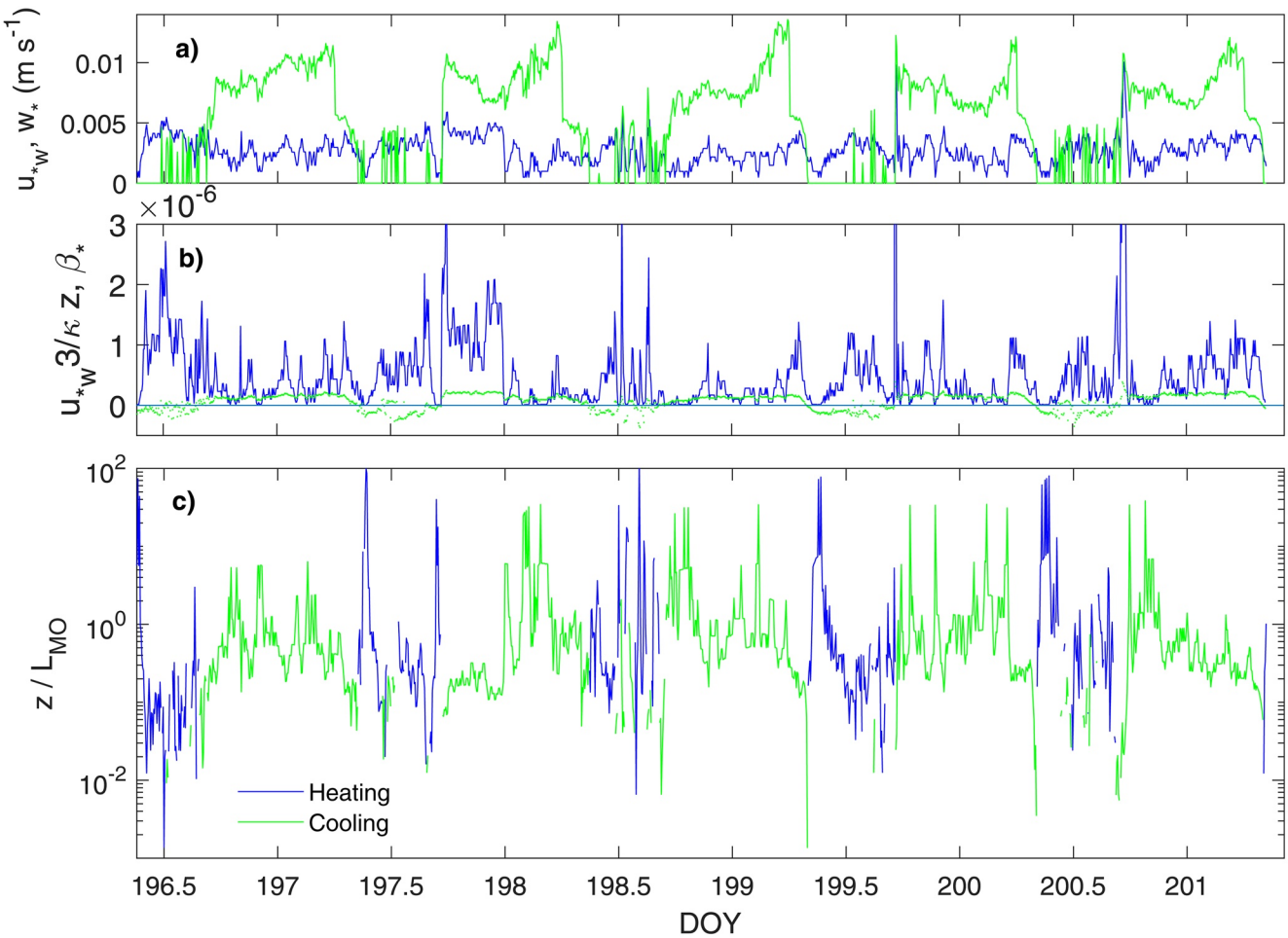

Figure 4. Time series of (a) u_{*_w} (blue), w_* (green), (b) ${u_{*_w}}^3/\kappa z$ (blue), that is, ε_s from law of the wall scaling, and effective buoyancy flux (β_*+, green dots) (m^2 s^{-3}), and (c) z/L_{MO} where L_{MO} is Monin-Obukhov length scale on the water side of the air-water interface. Heating (blue); cooling, with sign negative (green). Depth z is 0.15 m. The larger values of z/L_{MO} during light winds indicate that buoyancy flux will enhance dissipation rates over that predicted from law of the wall scaling at such times.

The water surface had ripples or small amplitude surface waves when we made our microstructure measurements (Table S1). Typically, when winds were less than 1 m s^{-1}, the water surface was rippled, as winds increased to 2 m s^{-1}, crest to trough wave amplitudes were 0.01–0.02 m, and as winds reached 3–4 m s^{-1}, crest to trough wave amplitude reached 0.2–0.3 m and occasionally 0.5 m. The spacing between wave crests varied from 0.2 to 1 m with the shorter distance as winds first picked up in the morning and during squalls and the larger distance as winds dropped. At times, ripples or low amplitude surface gravity waves occurred on lower frequency wave motions which we characterized as swell. Occasionally, 0.05 m surface waves were noted in the morning when winds were less than 1 m s^{-1}.

Langmuir cells were not observed. The estimated turbulent Langmuir number (La_T) was 0.55 (Figure 2c), indicating that conditions were such that they could form (McWilliams et al., 1997). If present, they could be the centimeter-scale Langmuir circulations observed by Veron and Melville (2001).

3.2. Profiles of Temperature-Gradient Microstructure

Microstructure profiling was conducted during heating when turbulence was shear-induced and during cooling when, although some near-surface shear was present, it was induced by penetrative convection through much of the upper mixed layer. The profiles captured the changes in the vertical overturning scales and dissipation rates associated with the set-up of the diurnal thermocline, the strong heating in early morning with continued heating through mid-day, the transitions associated with the wind-induced up and downwelling of the diurnal

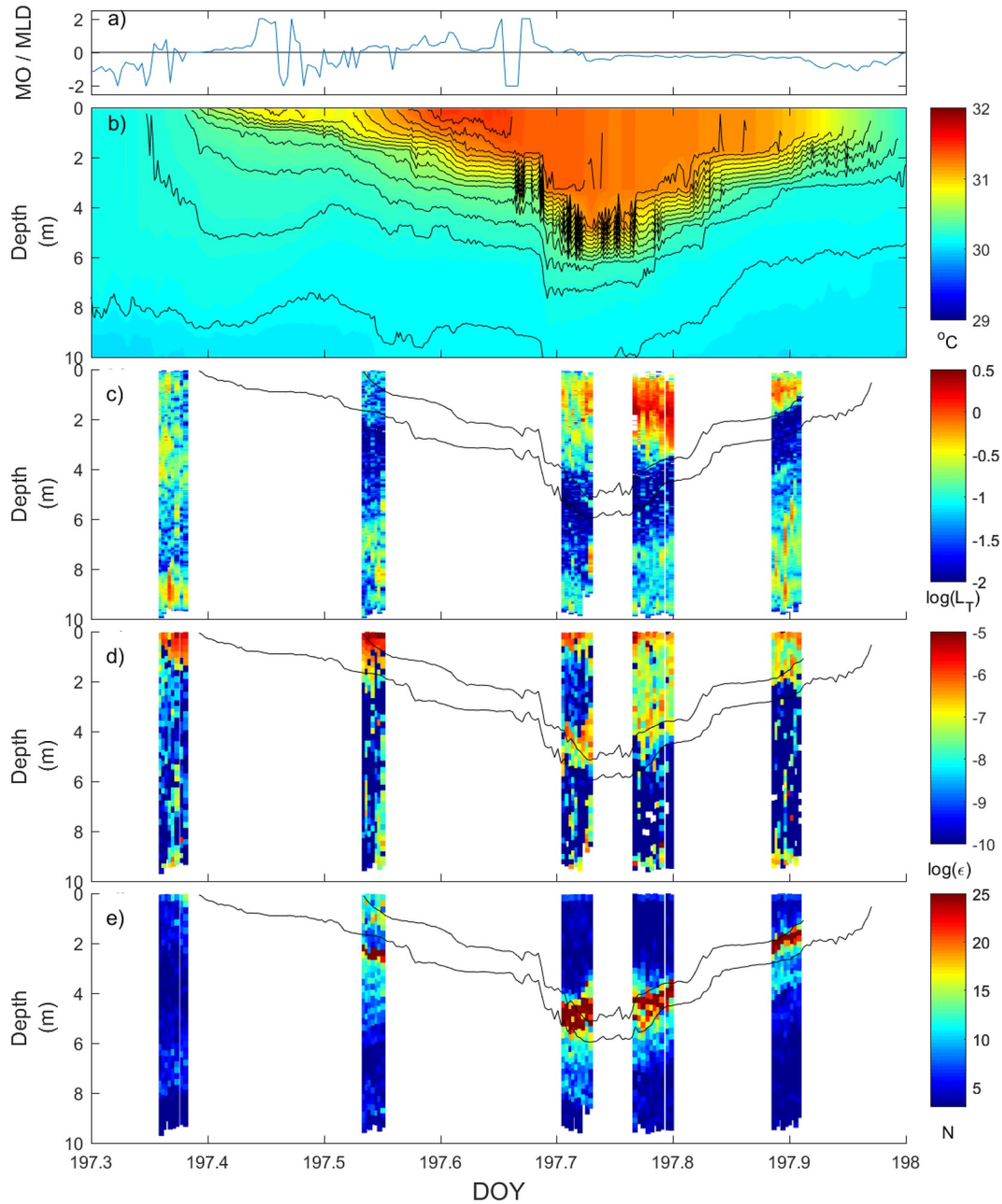

Figure 5. (a) Monin-Obukhov length scale (L_{MO}) divided by depth of the actively mixing layer (z_{AML}) (MO/MLD); (b) temperature contours at 0.02°C intervals overlaid by 2 min-averaged 0.1°C isotherms; (c) logarithm of centered Thorpe scales; (d) logarithm of rate of dissipation of turbulent kinetic energy (ϵ, $m^2\ s^{-3}$), and (e) buoyancy frequency N in cycles per hour for DOY 197 at the offshore site, Balbina Reservoir. Microstructure results in panels (c–e) are overlaid with 4 min averaged isotherms at 0.5°C intervals. *N* is scaled so that changes can be seen in near surface values.

thermocline, and the onset of cooling with convective mixing (Figures 5–8). Profiles were also obtained during penetrative convection before sunrise on DOYs 198 (Figure 6) and 201(data not shown). The transitions between heating and cooling are illustrated by the ratio of the Monin-Obukhov length scale to the actively mixing layer depth (L_{MO}/z_{AML}) (Figures 5a–8a). When negative, the actively mixing layer was cooling. Values near zero imply wind was dominating turbulence production only in a shallow near-surface layer whereas values larger than 1 imply turbulence in the actively mixing layer and in the water below was predominantly driven by wind. Although quantifying the depth of the actively mixing layer is challenging, with a few exceptions, the high resolution

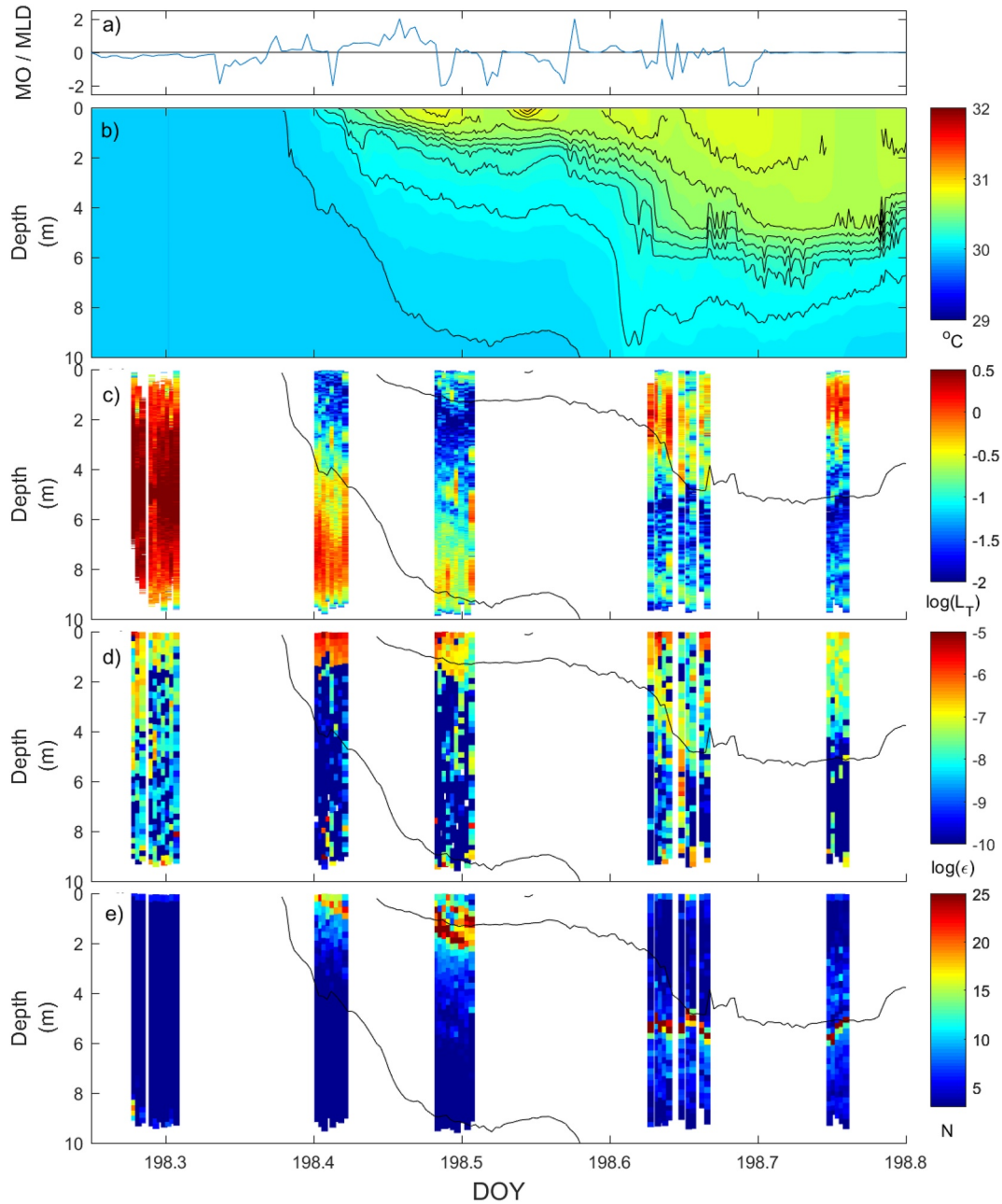

Figure 6. As for Figure 5 but for DOY 198.

temperature contours and isotherms support the interpretations as to whether the water column was heating or cooling based on L_{MO}/z_{AML} (Figures 5a, 5b–8a, 8b) as do the larger overturns (L_T) during cooling (Figures 5c–8c).

A striking feature is the high dissipation rates associated with the setup of the diurnal thermocline and the intensification of stratification within it (Figures 5–8). Dissipation rates in the upper 0.25 m typically exceeded 10^{-6} m^2 s^{-3} and occasionally reached 10^{-5} m^2 s^{-3}. Values were often highest at noon or shortly thereafter when stratification was pronounced. Near-surface dissipation rates were so sensitive to conditions of heating or cooling that they decreased by an order of magnitude with passing clouds, rain or the increased winds from squalls that led to near-surface cooling (e.g., ~DOY 198.5, 198.65, Figure 6d and DOY 199.7 Figure 7d).

The daily patterns varied with the sign of β. As some aspects are similar to those obtained in prior studies over diel cycles (Brainerd & Gregg, 1993; Soloviev et al., 2001; Tedford et al., 2014), we first briefly describe them

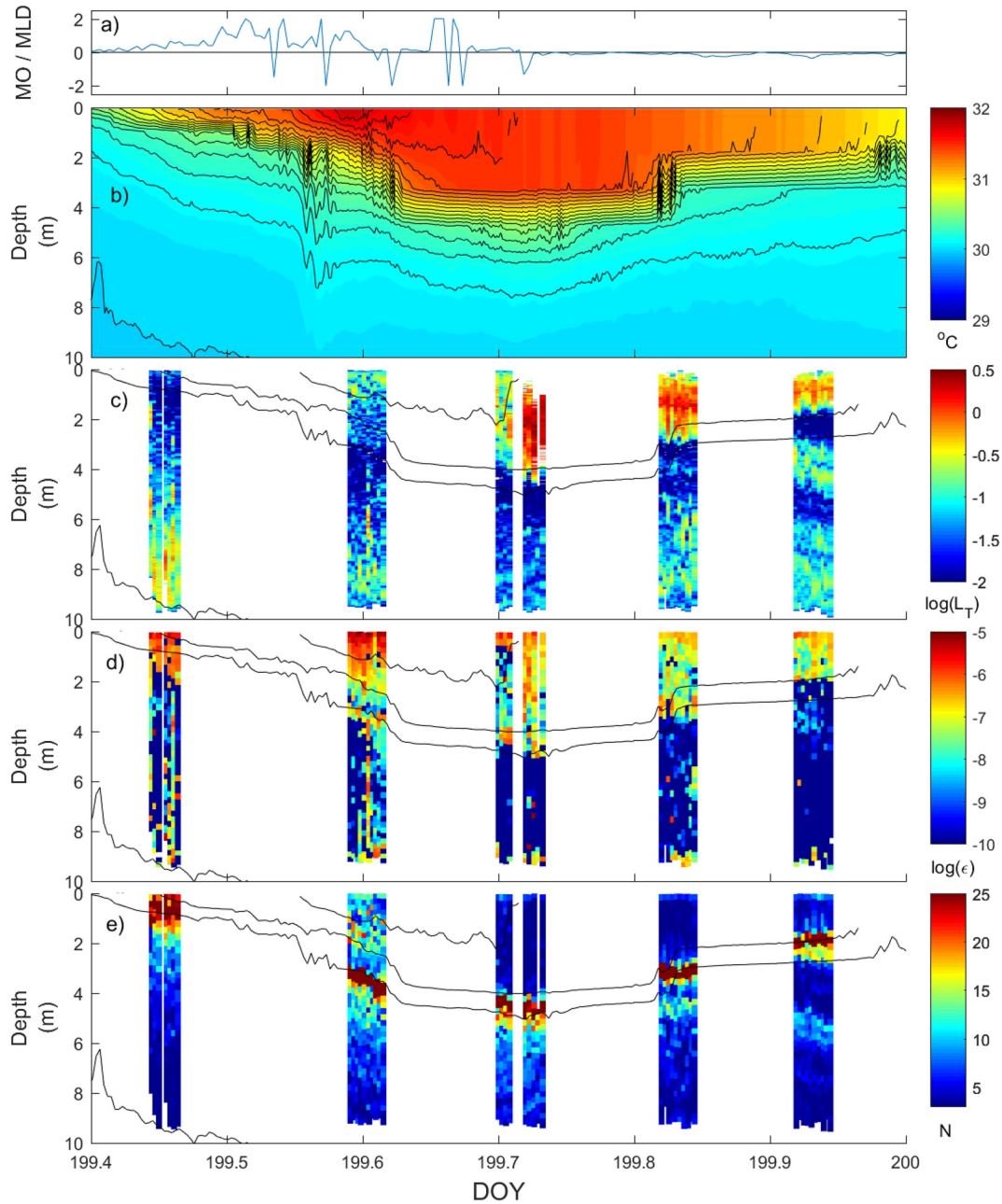

Figure 7. As for Figure 5 but for DOY 199.

here and then concentrate on the novel features. Prior to the onset of heating, overturning extended through the upper 10 m where we sampled. Dissipation rates were slightly elevated at the surface, with values typically near 10^{-7} m^2 s^{-3}, and lower below (Figure 6, DOY 198.3). With the onset of heating and development of near-surface stratification, overturns decreased in size in the upper water column, and larger overturns persisted for much of the day in the weakly stratified subsurface layer (Figures 5–8). During heating, dissipation rates were elevated near the surface but decayed and were often below detection in the subsurface layer. Once cooling began, overturns increased in magnitude near the surface. Near-surface dissipation rates decreased relative to the heating period but were elevated throughout the actively mixing layer.

The rapid changes in near-surface stratification and in dissipation rates in response to subtle changes in heating, cooling, wind speed and direction set the data from Balbina Reservoir apart from earlier studies. When the

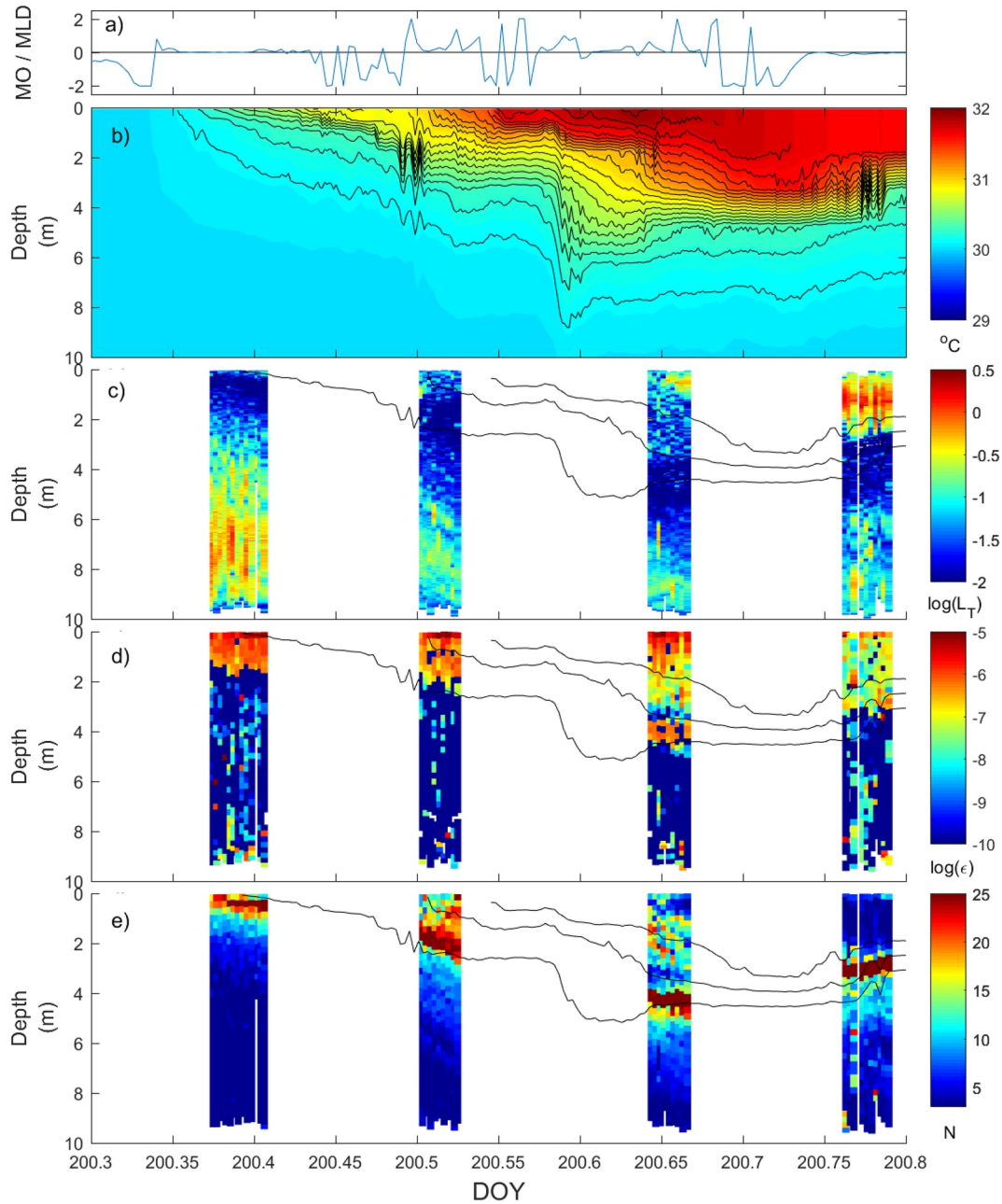

Figure 8. As for Figure 5 but for DOY 200.

near-surface diurnal thermocline extended to the surface, ε exceeded 10^{-7} m^2 s^{-3} and occasionally reached 10^{-5} m^2 s^{-3} in the upper 0.25 m. Near-surface stratification was often intense during morning heating with N sometimes reaching 25 cph (Figure 7e). Despite the strong stratification, dissipation rates often exceeded 10^{-6} m^2 s^{-3}. When wind increased slightly, as indicated by L_{MO}/z_{AML} increasing and with the descent of the diurnal thermocline, N decreased to ~10 cph as indicative of mixing. Dissipation rates remained elevated when near-surface N exceeded 5 cph (Figures 5–8). The highest values of ε occurred when L_{MO}/z_{AML} increased to values slightly above zero, indicating a slight increase in wind speed, stratification still extended to the surface, and N had weakened to ~10 cph. At such times, ε occasionally reached 10^{-5} m^2 s^{-3} due to the increased wind shear. The decrease in N was indicative of wind induced mixing. Such transitions can be seen during the first two profiling sessions on DOY 200 (Figure 8). When the wind shifted direction in the afternoon and cooling began, near-surface dissipation rates decreased relative to earlier values. They exceeded 10^{-7} m^2 s^{-3} where N > 5 cph in the upper meter, decreased

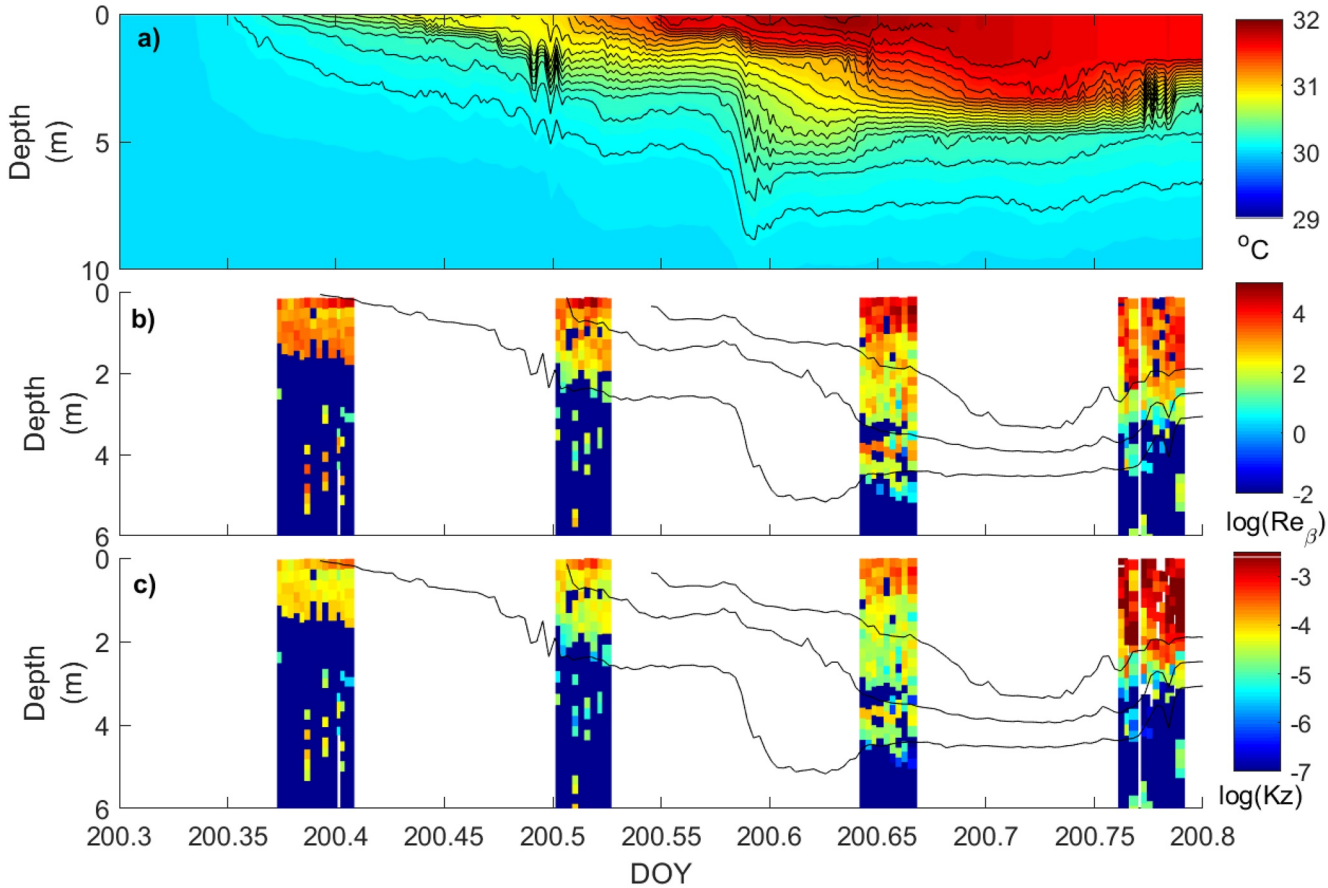

Figure 9. Time series on DOY 200 of (a) temperature, (b) buoyancy Reynolds number, Re_β, (c) coefficient of eddy diffusivity, K_z ($m^2\ s^{-1}$), with both Re_β and K_z on a logarithmic scale. When ε was less than $10^{-10}\ m^2\ s^{-3}$ or did not meet quality controls, values of Re_β and K_z were set to 0.01 and to $10^{-7}\ m^2\ s^{-3}$, respectively. K_z in the upper 3 m after DOY 200.75 uses the algorithm for cooling described in methods. Note, depth scale has been expanded for Re_β and K_z.

at depths below in the surface layer and diurnal thermocline, and were even lower in the weakly stratified water below (Figures 5–8). Overturns increased in size as is typical with mixing by convection (Tedford et al., 2014).

The diurnal thermocline began to descend with the slight increase in wind by late morning, Stratification within it was stronger than in the overlying water, with N ~ = 25 cph or higher: overturns within it were only a few centimeters. Dissipation rates increased above $10^{-7}\ m^2\ s^{-3}$ in the diurnal thermocline when internal wave activity was evident. Examples include the contraction of the diurnal thermocline on DOY 200.65 (Figure 8) or when the high frequency temperature oscillations indicative of high frequency waves were present as on DOY 197.7 (Figure 5).

The buoyancy Reynolds number, Re_β, was typically elevated above 500 as stratification developed in the morning indicating the turbulence was isotropic (Figure 9b). In the upper 0.25 m, it exceeded 10^4 frequently during heating and values increased as wind and dissipation rates increased and N decreased to ~10 cph (Figure 9). The highest values of Re_β near the surface occurred when heating was accentuated (e.g., DOYs ~200.4, 200.52 Figure 9), and values were similar near noon on other days (data not shown). Re_β was lower below the surface but still often above 500. Within the diurnal thermocline, Re_β was typically in the range 10^2 to 10^3. Values of order 10 or below occurred when there was a clear separation between a more energized upper mixing layer and the diurnal thermocline and at the base of the diurnal thermocline when rms overturning scales, L_T, were centimeter sized.

The coefficient of eddy diffusivity exceeded $10^{-4}\ m^2\ s^{-1}$ near the surface and was $\sim 5 \times 10^{-5}\ m^2\ s^{-1}$ in the upper 2–3 m during morning heating and mid-day (Figure 9c). When the diurnal thermocline downwelled, K_z in the upper 1–2 m remained $\sim 10^{-4}\ m^2\ s^{-1}$, but K_z was half a decade or a decade lower in the weakly stratified water below. K_z increased slightly in the diurnal thermocline when internal wave activity was evident, as during the

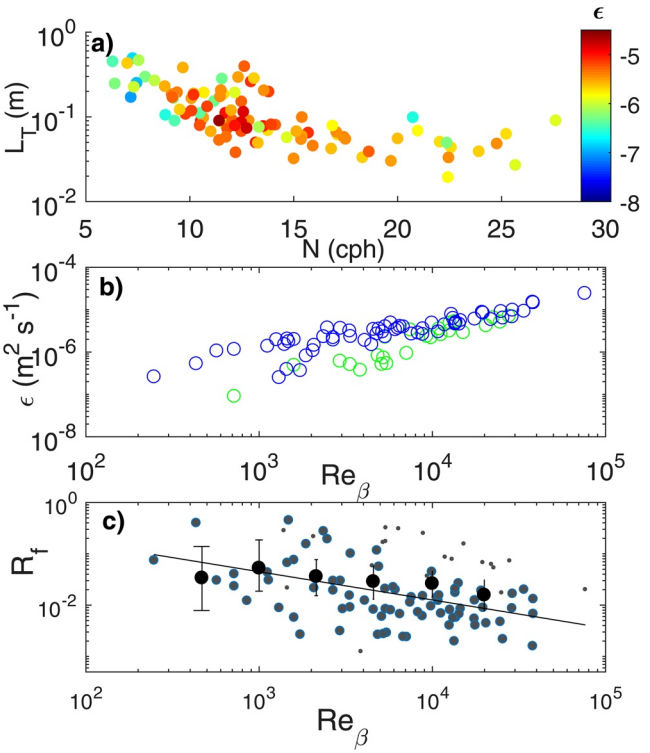

Figure 10. (a) Log of dissipation rate (ε [m^2 s^{-3}], dots) as it varies with buoyancy frequency (N, cph) and size of turbulent overturns as rms Thorpe scales (L_T); (b) Buoyancy Reynolds number (Re_β) and ε with blue dots indicating cases in which L_T was less than 0.12 m; (c) Re_β and flux Richardson number (R_f) with larger gray dots when dT/dz in the upper 0.12 m > 0.1°C^{-1}, black dots maximum likelihood estimates (MLE) of R_f in half decade bins and vertical lines the standard deviation for dT/dz criterion above, black line $R_f = 2Re_\beta^{-0.55}$ (Monismith et al., 2018). SCAMP data in all three panels are from the uppermost bin, ~0.25 m, during heating period from ~0830 to ~1530 hr.

compression event on DOY 200.65. Once cooling began, K_z increased appreciably above the diurnal thermocline. Values of K_z in the subsurface layer during the heating period were near molecular values.

3.3. Variability in Near-Surface ε and Re_β During Heating (0830–1530 hr)

Dissipation rates in the upper 0.25 m had maximal values, occasionally reaching ~10^{-5} m^2 s^{-3}, during the heating period when N was between 10 and 15 cph and Thorpe scales (L_T) were less than 0.4 m (Figure 10a). As N increased above 15 cph, dissipation rates decreased but most exceeded 10^{-6} m^2 s^{-3}. Dissipation rates tended to drop below 10^{-6} m^2 s^{-3} for N < 8 cph and L_T > 0.1 m. The larger eddies during weaker stratification occurred just as the water column began warming after dawn, when the diurnal thermocline downwelled with the shift back to easterly winds, and when clouds caused intermittent cooling. The buoyancy Reynolds number (Re_β) varied from 10^2 to 10^5. Values of Re_β > 200 imply the turbulent flow was isotropic (Gargett et al., 1984) and that the turbulence could be considered as energetic and developing (Shih et al., 2005). Dissipation rates increased with Re_β, which is in part to be expected as ε is the numerator in the equation (Figure 10b). However, distinct trends occurred for ε as a function of L_T. That is, for smaller L_T, ε was higher for a given Re_β until values converged for $Re_\beta \sim = 10^4$ and dissipation rates were 10^{-5} m^2 s^{-3}. The distinction between the two trends is more pronounced when the data during the cooling period are included in the graph (not shown). As N ~ = 12 cph at the convergence point, Figure 10b reiterates that maximal dissipation rates occur for moderate values of N. These higher values tended to occur when U_{10} > 3 m s^{-1}.

When near-surface dissipation rates were plotted in the Froude-Reynolds number diagram, samples during cooling had turbulent Froude numbers ranging from 0.6 to 1.6 whereas those obtained during heating ranged from ~1.6 to 10 (Figure S1). These patterns followed predictions for the ranges expected during penetrative convection and in diurnal mixed layers in Imberger and Ivey (1991). Dissipation rates varied in the two regimes, with those during cooling in the range 10^{-7} to 10^{-6} m^2 s^{-3} whereas ε during heating exceeded 10^{-6} m^2 s^{-3}. Maximal values occurred for Re_β of order 10^5 which can be calculated from the equality $Fr_T = (1/Re_T)^{1/2}$ $Re_\beta^{1/2}$. Flux Richardson numbers (R_f) are expected to be less than critical when Fr_T > 1.6 (Ivey & Imberger, 1991).

The flux Richardson number (R_f) ranged from 10^{-3} to 0.4 and decreased with increasing Re_β, although with some scatter as is to be expected for turbulent flows (Figure 10c). Most values were below 0.2. R_f > 0.3 occurred during brief intervals when temperatures at 0.05 m decreased. For U_{10} > 3 m s^{-1}, R_f was primarily in the range from 0.02 to 0.001. For $Re_\beta > 10^3$, maximum likelihood estimates tended to decrease albeit less steeply than the trend line in Monismith et al. (2018). Their regression was obtained from eddy covariance data in near-shore flows when buoyancy flux (b) was measured directly and is similar to that in Shih et al. (2005). Values of R_f in Balbina R. were predominantly lower than R_{fcrit} of ~0.2, unlike much of the oceanic data reported by Gregg et al. (2018). Ozmidov scales ranged from 0.1 to 1 m, such that $L_o/\kappa z > 1/4$, a regime in which Holleman et al. (2016) reported a decrease in R_f as Re_β increased. The low values of R_f imply a continued introduction of energy such that the turbulence had not evolved to a steady state and a low mixing efficiency (Shih et al., 2005; Smyth et al., 2019). The arithmetic mean of R_f for the heating period when the temperature gradient in the upper 0.12 m exceeded 0.1°C m^{-1} was 0.04.

3.4. Relation Between Dissipation Rates and ζ—Variability in φ_ε With Heating and Cooling

φ_ε increases from the value of 1 expected for law of the wall scaling by up to 3 orders of magnitude as z/L_{MO} increases from 0.01 to 100. For $\zeta < 0.1$, the MLE of φ_ε is 1, indicating the data follow law of the wall scaling. As ζ progressively increases, φ_ε increases with the MLE 10 times higher than 1 at $\zeta = 1$ and 100 times higher when $\zeta = 10$. The few data points for $\zeta = 100$ indicate φ_ε 1,000 times higher than predicted by law of the wall scaling. The largest scatter in φ_ε was in the range $0.1 < z\ L_{MO} < 1$. With only a few exceptions, rms overturn sizes were less than 0.12 cm

The relation between the MLE of φ_ε and ζ is captured with the equation $\varphi_\varepsilon = (1 + 22\ \zeta)$. The arithmetic mean of R_f for the heating period was 0.05 and when constrained with $dT/dz > 0.1°C\ m^{-1}$, 0.04. The inverse of the intermediate value, 0.045, is 22, in agreement with the regression.

Once $z/L_{MO} > 0.1$, the curve based on the regression of MLE of φ_ε versus z/L_{MO} for the upper 0.25 m exceeded predictions from models developed from experiments in stable atmospheres and near-surface waters of a stratified lake. With the exception of Tedford et al. (2014), these models follow law of the wall scaling for $\zeta < 0.1$, and φ_ε progressively increases as ζ increases. In all cases, the increase in observed φ_ε is larger for the data from Balbina *R*. Sutherland et al. (2016) found a fivefold increase in φ_ε relative to law of the wall scaling but ζ is not available. φ_ε in our study exceed predictions from Grachev et al.'s (2013) $\varepsilon/\varepsilon_s = (1 + 5\ \zeta)$, where 5 is the inverse of the critical flux Richardson number.

φ_ε, modeled as $1 + (1/R_f)\zeta$, where R_f was computed from Re_β following Monismith et al. (2018), increased with φ_ε and captured the scatter expected for individual R_f. However, φ_ε modeled in this manner often exceeded values obtained using the microstructure data. The larger values result from underestimating N, the denominator of Re_β, due to the 0.45 m separation of the upper two thermistors.

Soloviev et al. (2001) computed a similarity scaling in the upper mixed layer below the wave breaking zone in the upper 3 m. During heating, the upper mixed layer was often 20 m deep. They constrained their analysis to conditions when $u_* > 0.3$. In contrast, $u_* < 0.15$ in our data set except during two brief squalls. They presented their results relative to the gradient Richardson number and cover the range from 0.0 to 0.2. This range, when converted to ζ using their Equation 8 and critical $Ri = 0.25$, is equivalent to $0.001 < \zeta < 1$. Their mean values would fall on a curve similar to ours with variability in individual values increasing as gradient Richardson numbers increased. The similarity scaling here extends the range of ζ in their study.

φ_ε for the remainder of the upper mixing layer also increased with z/L_{MO} although the enhancement of φ_ε with increasing z/L_{MO} was less and collapsed to the scaling in Grachev et al. (2013) (Figure 12). In fact, when the data are fitted for the upper four ~0.25 m bins, B_A decreased from the surface downwards with $B_A = 23$, 7.5, 5.3, and 3.9 (Figure S2). For $B_A = 1/R_f$, the corresponding values of R_f would be 0.04, 0.13, 0.19, and 0.26, indicative of instability in the upper meter and more active turbulence near the surface. Histograms of $\log_{10}(Re_\beta)$ illustrate a steady decrease in range in the four bins in the upper meter with median values indicating isotropic turbulence and decreasing from 10,565, 9,771, 4,487, to 2,791 (Figure S3).

During the cooling period~1530–0830 hr, nonzero L_{MO} implies that shear was the primary driver of near-surface turbulence (Figures 3, 5–8). Estimates of φ_ε were primarily in the range from $-0.1 < \delta < -10$ and were ~ five times higher or lower than expected from law of the wall scaling (Figure 13). Values less than law of the wall scaling for $|\zeta| < 0.6$ occurred the evening of DOY 197 when wind speeds were higher than on other nights, on DOY 199 when they rose over the course of 14 min from 2.5 to 4 m s^{-1}, and on two other days when the shift occurred from westerly to easterly winds and wind speeds increased from 0.5 m s^{-1} to 3.5 or 7 m s^{-1} in ~15 min. With such abrupt changes, shear may not have been fully developed. On rapidly falling winds, φ_ε was sometimes 7 times higher than predicted, indicating continuation of the shear which had previously developed. Anomalies also occurred when winds were light. $\varphi_\varepsilon > 7$ when $|z/L_{MO}| > 5$ occurred under light winds with a rippled surface and $\varphi_\varepsilon > 5$ when $|z/L_{MO}| \sim = 0.7$ occurred when winds were light and the surface was rippled with an underlying swell. These discrepancies point to other processes moderating shear near the surface. For the 3 bins in the range $-2 < z/L_{MO} < -0.06$, where data were sufficient for maximum likelihood estimates to be calculated, the fit was somewhat better with the Wyngaard and Coté (1971) than the Tedford et al. (2014) model. Increases in φ_ε relative z/L_{MO} make a smaller contribution to ε under cooling than under heating (Figures 11 and 13).

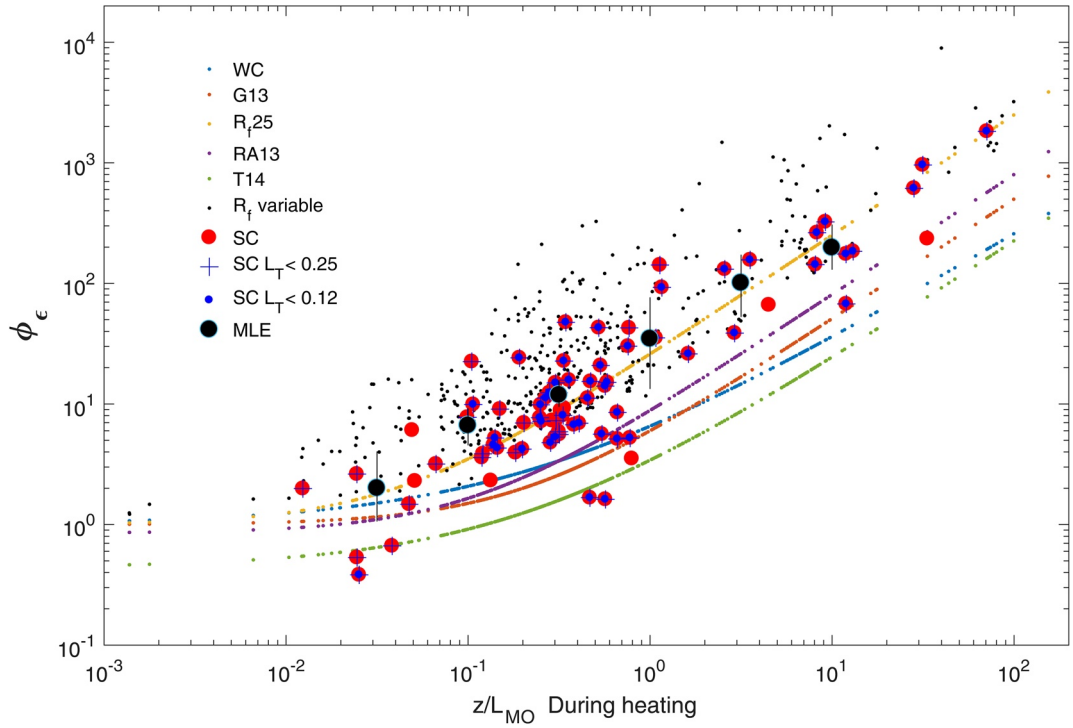

Figure 11. Change in φ_ε under heating (~0830–1530 hr) for increasing $z/L_{MO.}$ $\zeta = z/L_{MO} = 0.4z\beta_*/u_{*_w}{}^3 = \beta_*/\varepsilon_s$. φ_ε for the SCAMP data were determined by dividing measured ε by ε_s (red dots), values when $L_T < 0.25$ overlaid by a black cross ($L_T < 0.25$), and values when $L_T < 0.12$ overlaid with blue dots. We let $z = 0.15$ m as that is approximately the mid-point of the upper most bin of the SCAMP data and enables comparisons with equations describing similarity scaling under heating. MLE and standard deviation (black dots and error bars). Modeled φ_ε using equations of Wyngaard and Coté (1971) (WC, blue dots), Grachev et al. (2013) (G13, brick red dots), Sanz Rodrigo and Anderson (2013) (RA13, purple dots), Tedford et al. (2014) (T14, green dots), Curve for $R_f = 0.04$ is shown (yellow dots; nearly identical to that for $R_f = 0.045$); model for R_f variable (this study—computed Re_β from meteorological and time series temperature data, black dots). $z = 0.15$ m for all model results and computations are based on our time series meteorological and temperature data.

3.5. Variability of Terms Used to Model ε for Different Ranges of Wind Speed

Variability of the terms used to model ε are illustrated in Figure 14. Under cooling, β_* progressively becomes more negative with increased wind speed (Figure 14a). However, under heating, maximal values of β_* were independent of wind speed. Drag coefficients at instrument height increased as wind speed decreased (Figure 14b). Values for each wind speed range were higher during cooling, implying that the atmosphere was more unstable under those conditions. As expected given the definition of L_{MO}, the ratio $|z/L_{MO}|$ decreases as $|\beta_*|$ approaches zero implying a progressive decrease in the contribution of β_* to turbulence production (Figures 14c and 14d). Law of the wall scaling would only apply at the wind speeds obtained during the brief squalls or as β_* approached 0. z/L_{MO} increased by ~2 decades as wind speeds decreased from values larger than 4 m s^{-1} to less than 2 m s^{-1}. R_f varied from 10^{-3} to 0.4 with no clear dependence on β_* or wind speed (Figure 14e). As U_{10} increased from 0 to 8 m s^{-1}, ε_s increased from 10^{-9} to 10^{-5} m^2 s^{-3}. The calculation of u_{*_w} used to compute ε_s incorporates the larger C_D as occurs when the atmosphere is unstable. That ε is larger than ε_s under heating results from the contribution of these various terms to dissipation in the water column (Figures 11 and 13).

3.6. Near-Surface ε and k_{600} as Functions of Wind Speed and Buoyancy Flux

During heating, MLE of ε computed from the SCAMP data averaged ~5×10^{-6} m^2 s^{-3} for U_{10} from 0.5 to 3.5 m s^{-1} and were independent of wind speed (Figure 15a). MLEs from the SCAMP data overlap ε modeled as $\varepsilon = \varepsilon_s \cdot (1 + 1/R_f \cdot z/L_{MO})$ when R_f is the arithmetic mean (0.04) and the temporally varying value computed from Re_β. Dissipation rates from the SCAMP exceed those obtained following the models of Grachev et al. (2013) and Tedford et al. (2014). Similarly, MLE of k_{600} calculated using the surface renewal model and ε calculated from

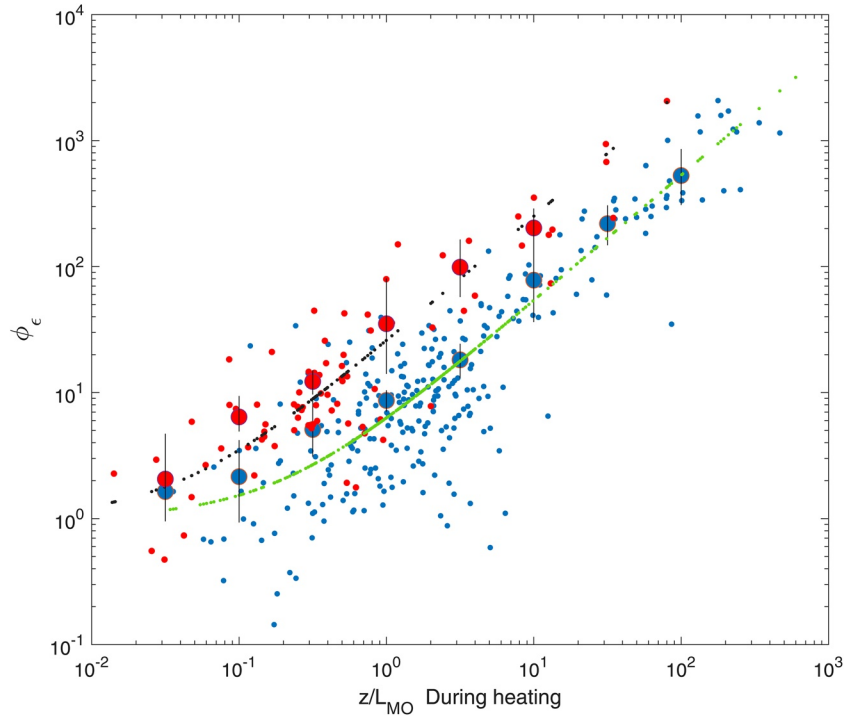

Figure 12. φ_ε under heating (~0830–1530 hr) as it varies with z/L$_{MO.}$ φ_ε for the SCAMP data in the upper most bin as in Figure 11 (red dots) and for the bins below it within the actively mixing layer (blue dots). MLE and standard deviation as in Figure 11. The curve for the uppermost bin (black dots) follows $\varphi_\varepsilon = 1 + 23$ z/L$_{MO}$; the curve for the remainder of the actively mixing layer (green dots) follows $\varphi_\varepsilon = 1 + 5$ z/L$_{MO}$ as in Grachev et al. (2013). Mid-point of each bin was used for depth in these calculations.

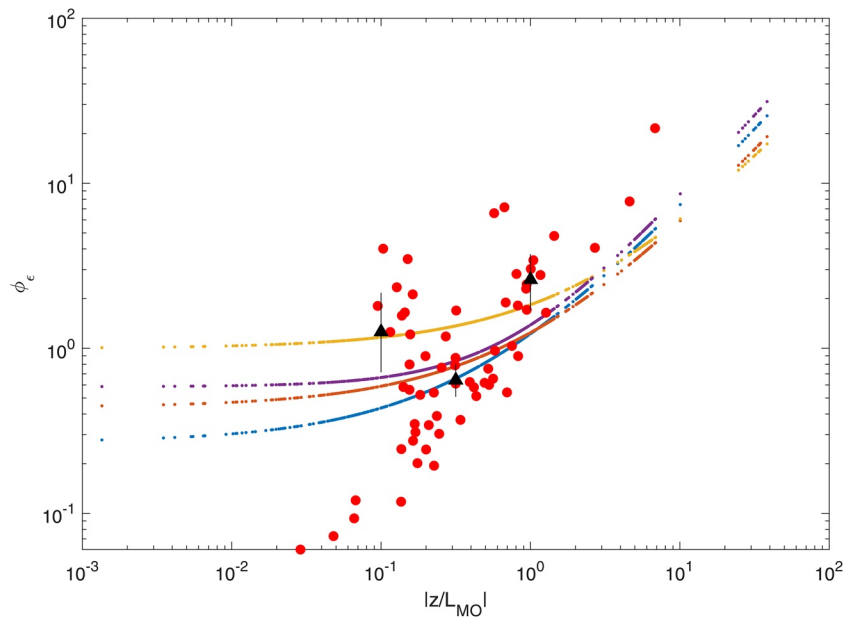

Figure 13. Change in φ_ε, computed from SCAMP data under cooling (red dots; from ~1530 to ~0830 hr the following morning and wind directions between 50° and 150°, for increasing |z/L$_{MO}$|. z/L$_{MO}$ is negative under cooling. Calculations are as in Figure 11 and constrained to times when U$_{10}$ > 0.5 m s^{-1} and $\beta_* < -0.1 \times 10^{-7}$ m^2 s^{-3}. Modeled predictions are for Wyngaard and Coté (1971) (yellow), and Tedford et al. (2014) Equation 2 (purple) and Tedford et al. (2014) Equation 1 for lower wind speeds ($u_{*_w} = 0.007$ m s^{-1}) (red) and all wind speeds in the study (blue). MLE of φ_ε are restricted to the range $-5 \times 10^{-2} > \zeta > -5$ and indicate only a minor increase in dissipation rates due to β_* during cooling.

the SCAMP data overlap values obtained using ε obtained from the two R_f models and exceed predictions based on the Grachev et al. (2013) and Tedford et al. (2014) models (Figure 15b). Modeled estimates of k_{600} from the SCAMP data are considerably in excess of those computed using the wind-based models of Cole and Caraco (1998) and Wanninkhof (1992) (curves not shown). The former has an intercept of 2 cm hr^{-1} and the latter has an intercept of 0 cm hr^{-1} and both increase to 4 cm hr^{-1} at U_{10} of 4 m s^{-1}.

Under cooling, maximum likelihood estimates of ε and k_{600} computed from the SCAMP data showed a slight increase with wind speed from 1.0 to 3.5 m s^{-1} with ε approximately an order of magnitude lower than values obtained during heating (Figures 15 and 16). It is not possible to identify whether the Wyngaard or Coté (1971) or the Tedford et al. (2014) model is more accurate. Again, calculated values of k_{600} exceed those predicted from the Cole and Caraco (1998) and Wanninkhof (1992) wind-based models as described above.

Maximum likelihood estimates of ε and of k_{600} increased linearly with buoyancy flux once β_* exceeded -1.5×10^{-7} m^2 s^{-3} (Figure 17). Dissipation rates increased from 4×10^{-7} m^2 s^{-3} under cooling to 10^{-5} m^2 s^{-3} when β_* reached 2×10^{-7} m^2 s^{-3}. Measured dissipation rates exceeded the predicted $0.8|\beta_*|$ for cooling in the absence of wind (Tedford et al., 2014, Equation 2). MLEs of k_{600} increased from 5.5 cm hr^{-1} under cooling to 12 cm hr^{-1} under the strongest heating for which we have sufficient SCAMP casts for averaging.

3.7. Variability in k_{600} With Wind Speed

The implications of the larger φ_ε on k_{600} during heating are apparent when contrasting k_{600} computed using the Grachev et al. (2013) and the variable R_f models for different ranges of z/L_{MO} (Figure 18). Here k_{600} was computed from the surface renewal model with time-series meteorological and temperature data using $\varepsilon = \varepsilon_s(1 + 5\ z/L_{MO})$ (Grachev et al., 2013) and $\varepsilon = \varepsilon_s(1 + 1/R_f\ z/L_{MO})$. For the Grachev et al. (2013) model, expected k_{600} range from 2 to 8 cm hr^{-1} (Figure 18a). With variable R_f, expected k_{600} range from ~8 to 18 cm hr^{-1}, similar to values we obtained with our chamber measurements under heating (Figures 18b and 19d). Both models illustrate that k_{600} can be independent of wind speed for winds less than 4 m s^{-1} during heating with variable z/L_{MO}.

3.8. Time Series of Measured and Computed ε and k_{600}

Near-surface dissipation rates computed from the microstructure data were enhanced by one to two orders of magnitude during heating relative to cooling for similar variability in z/L_{MO} and by ~ an order of magnitude for similar wind speeds (Figures 19a–19c). The variability of the dissipation rates computed from the SCAMP data is captured by combining the R_f model of ε for the heating period with the Wyngaard and Coté (1971) model during cooling (Figure 19c). Comparison of the calculated and modeled ε with law of the wall scaling further illustrates the increased dissipation rates in response to changes in z/L_{MO} (Figures 19b and 19c). During morning heating, ε was enhanced by one to three orders of magnitude relative to law-of-the wall scaling, the same period as noted by Hughes et al. (2020b) but with the enhancement up to an order of magnitude higher than they observed. The enhancement during cooling was at most a factor of five. The largest difference between calculated and modeled dissipation rates occurred during cooling on DOY 197 when winds were higher than on most other nights and φ_ε was lower than expected from law of the wall scaling (Figures 3, 5, and 13). Modeling ε with the mean value of R_f, such that $\varepsilon = \varepsilon_s(1 + 25\ z/L_{MO})$, captures a considerable portion of the variability observed in the measured ε but underestimates the highest measured values (data not shown).

Gas transfer velocities obtained with the chambers (k_{600ch}) during heating ranged from 8 to 18 cm hr^{-1}, similar to the values illustrated in Figure 18b and considerably higher than obtained with a commonly used wind-based model (Figure 19d). Values of k_{600ch} were similar to those computed using the surface renewal model using calculated and modeled dissipation rates further supporting our modeling approach and indicating that the variable R_f model captures the increased dissipation rates which occurred under heating with light winds. k_{600} during heating (cooling) was four to five (two) times higher than predictions from a commonly applied wind-based model (Cole & Caraco, 1998). The wind-based equations of Wanninkhof (1992) and McGillis et al. (2001, 2004) also did not capture the enhancement during the heating period (data not shown).

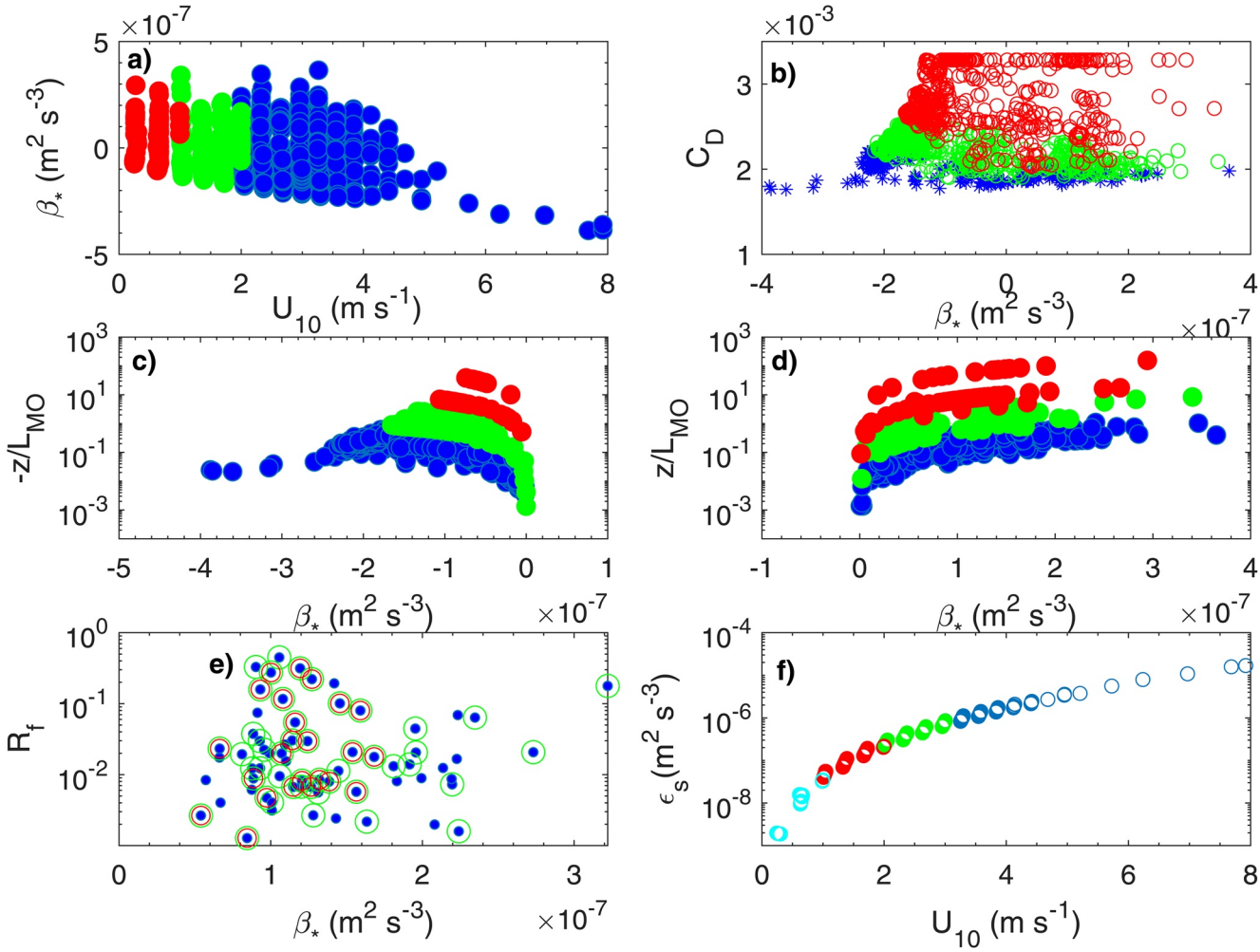

Figure 14. (a) Buoyancy flux (β_*) versus U_{10}: (b) drag coefficient at instrument height (C_D) versus β_*: (c) z/L_{MO} under cooling versus β_* where z is 0.15 m; (d) as for c but under heating; (e) flux Richardson number (R_f) from SCAMP data versus β_*, (f) ε_s, that is, ε from law of the wall scaling, versus U_{10}. Colors indicate ranges in wind speed. Cyan, $U_{10} < 1$ m s^{-1}; Red, $U_{10} < 2$ m s^{-1}; Green, $U_{10} < 3$ m s^{-1}; Blue, $U_{10} \geq 3$ m s^{-1}. In $|z/L_{MO}|$ panels, there is some overlap of values in the range $U_{10} \geq 3$ m s^{-1} with those for U_{10} near 2 m s^{-1}. Due to considerable overlap of R_f, different marker sizes and extent of fill are used to discriminate U_{10} ranges in panel (e) Note, points overlap for different wind speed ranges in panels (b–d) but the trends are apparent.

4. Discussion

Instrumentation that can probe near the air-water interface in oceans and lakes enables improved understanding of the physical processes that induce fluxes of momentum, heat and dissolved gases (Hughes et al., 2020a, 2020b; Soloviev et al., 2001; Sutherland et al., 2016). Here, we used an upwardly rising temperature-gradient microstructure profiler to quantify dissipation rates in 0.25 m bins in the upper mixed layer, and coupled these measurements with time-series meteorological and temperature measurements. The enhancement of ε by buoyancy flux during heating over that expected from law of the wall scaling (φ_ε) in the upper 0.25 m of a tropical reservoir is well described by similarity scaling with the model $\varphi_\varepsilon = (1+(1/R_f)\ z/L_{MO})$. In atmospheric models, the maximum value of $1/R_f$ is 5, which is equal to the inverse of the critical flux Richardson number (Grachev et al., 2013). Here we found that the arithmetic mean of R_f in the upper 0.25 m was ~0.04 such that the multiplier on z/L_{MO} is ~five times higher. However, R_f varied from 0.001 to 0.4, and the variability in dissipation rates is captured when φ_ε is modeled using variable R_f. The increases we obtained in φ_ε as z/L_{MO} increased were similar to those below the zone of breaking surface waves in Soloviev et al. (2001); our analysis extends the range of z/L_{MO} that they investigated. Below the upper 0.25 m, the similarity scaling collapses to that of Grachev et al. (2013). The measurements illustrate that the combination of the often high z/L_{MO} under light winds (Figures 14c and 14d) and the low R_f near the air-water interface (Figure 10c) contribute to elevated φ_ε such that dissipation rates exceed those estimated

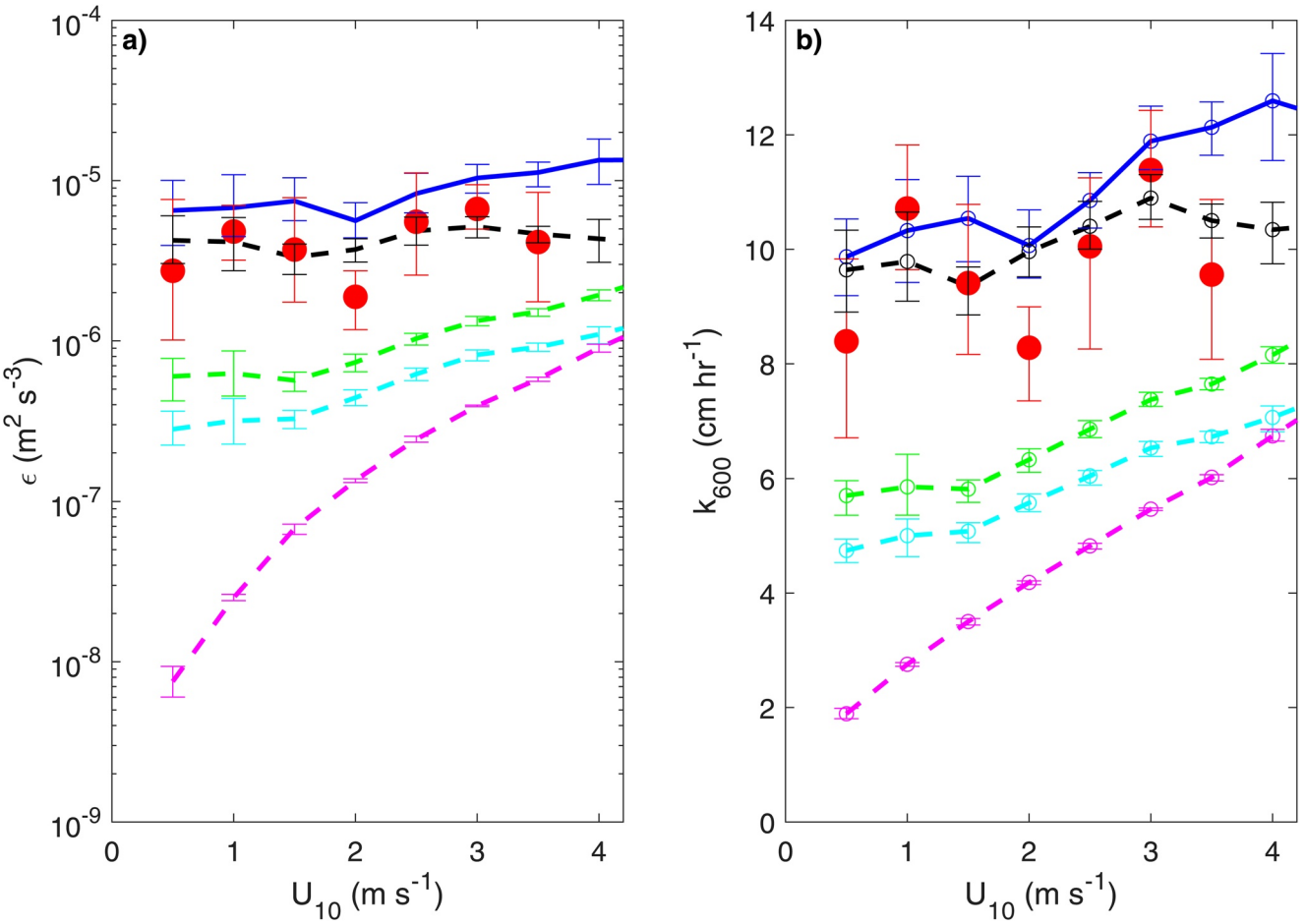

Figure 15. Heating period. (a) ϵ versus U_{10} for ϵ calculated from SCAMP measurements (red dots) and five models. Modeled $\varepsilon = \varepsilon_s \cdot (1 + 1/R_f \cdot |z/L_{MO}|)$ where R_f varies over time (blue), $\varepsilon = \varepsilon_s \cdot (1 + 25 \cdot |z/L_{MO}|)$ (black) where 1/25 is the arithmetic mean value of R_f for $Re_\beta > 10^2$ and $< 10^5$ (Figure 10c); $\varepsilon = \varepsilon_s \cdot (1 + 5 \cdot |z/L_{MO}|)$ (Grachev et al., 2013, green); $\varepsilon = \varepsilon_s \cdot (0.44^{2/3} + 2.2^{2/3} \cdot |z/L_{MO}|^{2/3})^{3/2}$ (Tedford et al., 2014, Equation 1 light winds, cyan); $\varepsilon = 0.6\ \varepsilon_s$ (Tedford et al., 2014, Equation 2, magenta). (b) k_{600} versus U_{10} with k_{600} computed from the surface renewal model using calculated and modeled dissipation rates as in panel (a). MLE (dots) and 95% confidence intervals (vertical lines).

from law of the wall scaling by up to 3 orders of magnitude (Figures 11, 15a, and 19c). In consequence, gas transfer velocities are considerably elevated during heating at low to moderate wind speeds (Figures 15b, 18, and 19d).

Our results support McGillis et al.'s (2004) suggestion, derived from their work in the equatorial Pacific Ocean over diel cycles with moderate winds, that biogeochemical models used in regional and global carbon models need to take into account the biological and physical processes that moderate near-surface stratification. With the increasing warming of lakes and oceans (Amaya et al., 2020; Frölicher et al., 2018; O'Reilly et al., 2015) and the likely enhancement in near-surface ϵ and k_{600} as illustrated here, doing so is even more urgent.

In the following, we further evaluate the reasonableness of our assumption that the variability in φ_ε can be explained using Monin-Obukhov similarity theory. We do so via calculation of near-surface shear using MOST, with comparisons to other studies, and with evaluations of the influence of surface waves.

4.1. Near-Surface Shear

We posit that the considerable enhancement in φ_ε in the upper 0.25 m the tropical reservoir relative to other studies in stable boundary layers is associated with enhanced near-surface shear. In oceanic studies, enhanced near-surface shear is associated with a diurnal jet found adjacent to and below the air-water interface (Hughes et al., 2020a; Price et al., 1986; Soloviev & Lukas, 2006). This feature begins as soon as stable stratification

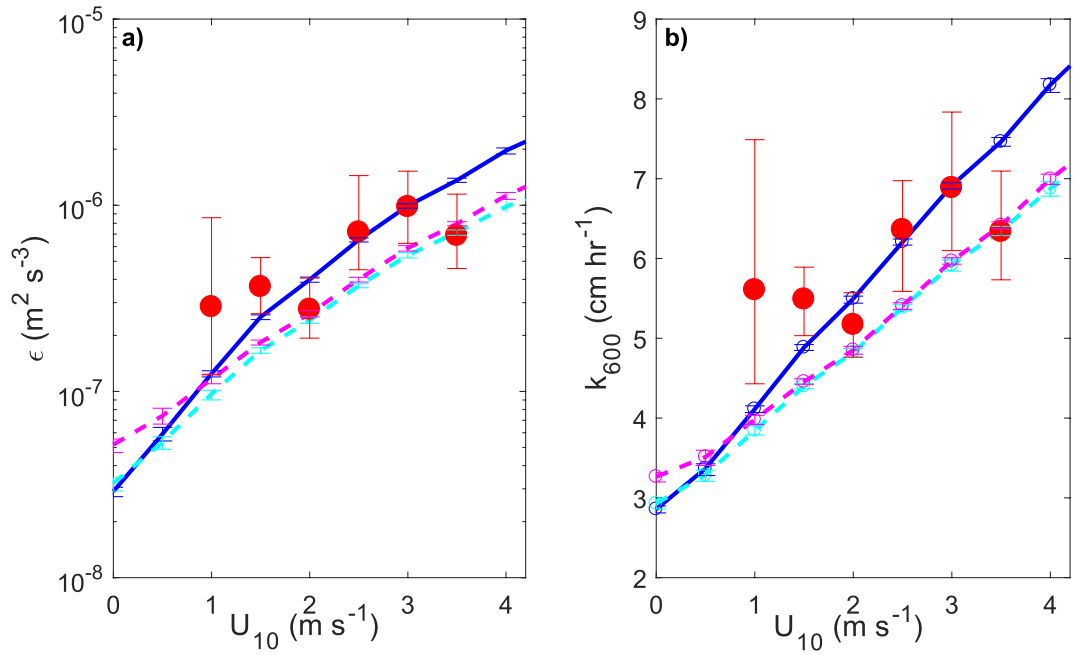

Figure 16. Cooling period. (a) ε from microstructure data (red dots) and models versus wind speed at 10 m height (U_{10}). Models: $e = \varepsilon_s$ (1 + 0.5 |z/L_{MO}|$^{2/3}$)$^{3/2}$ (Wyngaard & Coté, 1971; blue); $e = \varepsilon_s$ (0.44 $^{2/3}$ + 0.44 $^{2/3}$ |z/L_{MO}|$^{2/3}$)$^{3/2}$ (Tedford et al., 2014, Equation 1, light winds; magenta); $\varepsilon = 0.6\ \varepsilon_s$. + 0.77 |$\beta_o$| (Tedford et al., 2014, Equation 2, cyan). (b). k_{600} versus U_{10} with k_{600} computed from the surface renewal model using ε from microstructure data and models as in panel (a) Dots and vertical lines as in Figure 15. Analysis is for cooling conditions prior to 0830 hr and after 1530 hr when β_* and z/L_{MO} are negative.

develops in the day and its velocity increases as the diurnal thermocline shoals (Soloviev & Lukas, 2006). Increases in dissipation rates in the diurnal jet are similar to our observations. That is, Sutherland et al. (2016) found ε in the upper 0.5 m in excess of 10^{-6} m^2 s^{-3} and up to 5 fold higher than expected from law of the wall scaling. Hughes et al. (2020b) obtained ε_T, that is thermal dissipation rates, 100 fold higher than expected from law of the wall scaling during light winds. We obtained a larger enhancement of φ_ε in the upper 0.25 m than in the remainder of the upper mixing layer in our study (Figures 12 and S2). Thus, our calculated dissipation rates are similar to those found during heating in oceanographic studies of near-surface turbulence when a diurnal jet was present. These comparisons suggest near-surface shear would be elevated in the tropical reservoir although determining whether a diurnal jet is present would require additional work.

To estimate near-surface shear, we use the equality φ_m (1-R_f) = φ_ε and the definition $\varphi_m(\zeta) = (\kappa z/u_{*_w})du$/dz (Grachev et al., 2013, 2015). This approach assumes the turbulent kinetic energy budget is steady and that ε exceeds the buoyancy flux (b) within the layer and the vertical transport term (Section 1.1). Our estimates of φ_m used to calculate near surface shear are similar for the comparable ranges of z/L_{MO} in our work and Soloviev et al.'s (2001). Their similarity scaling is based on Richardson numbers, which when converted to ζ extend to a value of 1. Their microstructure data were obtained with a vertically rising shear probe hence are independent of the assumption of near equality of φ_m and φ_ε required for our analysis. The equivalence of our results and theirs implies that our results were obtained at depths where similarity scaling is expected to apply, that is, below the wave breaking zone, and that our use of the simplified TKE budget was justified.

Dissipation rates near the surface during wave breaking scale with $u_{*_w}{}^2 c_b H_s$ where c_b depends on phase speed, c_p = sqrt(g/k) and $k = 2\pi/\lambda$ where λ is wavelength and k is wavenumber, and H_s is significant wave height (Terray et al., 1996). H_s can be calculated as four times the square root of mean square elevation estimated as a function of fetch and u_* as in Csanady (2001). Based on that analysis, we obtain an upper bound of 0.04 m for H_s. Using the shorter and longer wavelengths estimated in the field, 0.3 and 1 m, resultant c_p = 0.7 and 1.2 m s^{-1}, and following Terray et al. (1996), we obtain $c_b = 0.5\ c_p$. We obtain values of $\varepsilon H_s/u_{*_w}{}^2 c_b$ less than 0.001 regardless of wavelength, indicating that breaking surface waves were not contributing to enhanced dissipation rates in the upper 0.25 m. Thus, these calculations imply data were obtained at depths in which turbulence production was

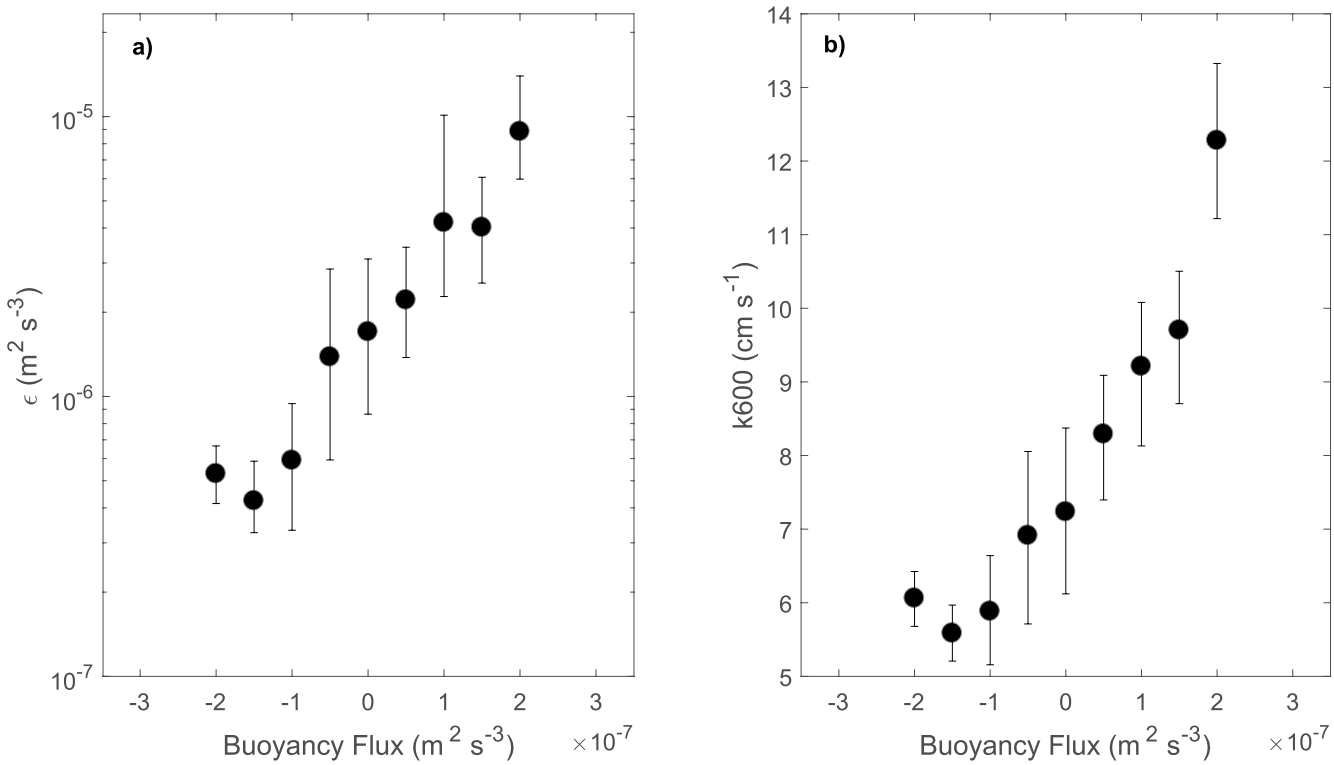

Figure 17. (a) ϵ from microstructure measurements versus buoyancy flux into the actively mixing layer (β_*); (b). k_{600} calculated using the surface renewal model and dissipation rates in panel (a). Maximum likelihood estimates (black dots) and 95% confidence intervals (vertical lines). Buoyancy flux is linearly related to heat flux. Here, an effective heat flux of −300 W m^{-2} is equivalent to $\beta_* = -2.2 \times 10^{-7}$ m^2 s^{-3}, and an effective heat flux of 300 W m^{-2} is equivalent to $\beta_* = 2.2 \times 10^{-7}$ m^2 s^{-3} (Figures 2g and 3a).

dominated by shear. That said, shear associated with orbital velocities of surface waves or Stokes drift may contribute to wind-driven shear.

Estimated shear in the upper 0.25 m increased from 0.01 to 10 s^{-1} as z/L$_{MO}$ increased from 10^{-2} to 10^2 and N increased from 5 to 25 cph (Figure 20). The highest values occurred during morning heating with low winds and the absence of clouds. Shear ranged from 0.02 to 1 s^{-1} for winds greater than 3 m s^{-1}. Yeates and Imberger (2004) report shear ranging from 0.1 to 0.7 s^{-1} in L. Kinneret, Israel, 2 m below the surface; corresponding wind speeds and buoyancy flux are not available. In oceanographic studies with similar surface buoyancy flux and wind speeds up to 5 m s^{-1}, near-surface shear using ADCPs with ~0.1–0.5 m bins was ~0.03 s^{-1} (Shcherbina et al., 2019; Sutherland et al., 2016). Near-surface stratification tended to be lower in the oceanographic studies; Sutherland et al. (2016) report N ranging from 1 to 18 cph with lower values predominating. Our higher values of shear may be reasonable given that they were obtained under stronger stratification. Sutherland et al. (2016) obtained similar values of the gradient Richardson number near the surface as the values of R_f we obtained, and given that Ri$_g$ and R_f have nearly a 1:1 relation below the critical value of 0.25 (Grachev et al., 2013; Venayagamoorthy & Koseff, 2016), this correspondence also supports modeling shear assuming near equivalence of φ_m and φ_ε. That said, wind is often spatially variable at light winds, and flows from elsewhere may have contributed to the shear.

Although the surface buoyancy flux was similar in our study to the oceanographic ones, the overall increase in temperature with each morning's heating was as high as 2°C in Balbina R. in comparison to the 0.5°C in the other studies. This difference results from the lower winds after sunrise such that incoming heat is stored in a shallow layer. Higher diffuse attenuation coefficients (k_d) may also contribute to the increased heating, as open ocean sites are more likely to have k_d of order 0.01 to 0.1 m^{-1} whereas in the offshore waters of Balbina R. k_d was 0.5 m^{-1}. Thus, the greater heating of near-surface waters in Balbina R. combined with lower wind speeds relative to the other studies supports the high computed values of shear when z/L$_{MO}$ was greater than 10.

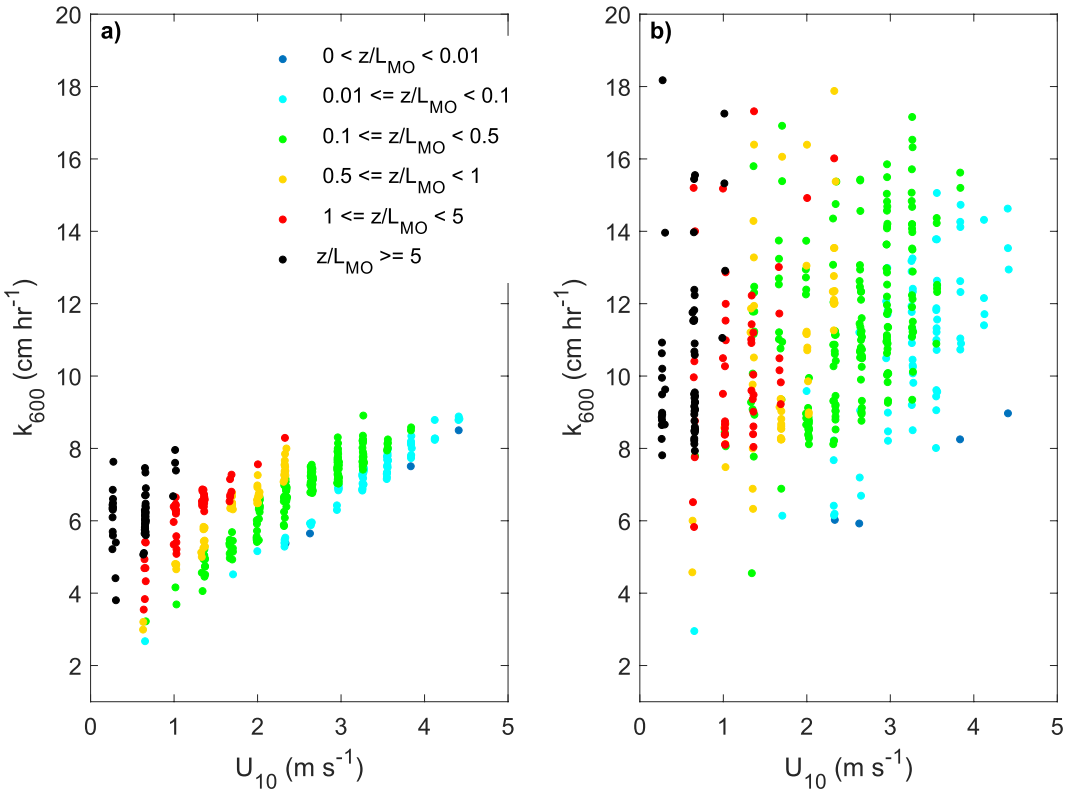

Figure 18. k_{600} computed from the surface renewal model versus U_{10} for various ranges of z/L_{MO} during heating where ε was calculated using the time series temperature and meteorological data following (a) Grachev et al. (2013) and (b) $\varepsilon = \varepsilon_s(1 + 1/R_f\, z/L_{MO})$ using variable R_f.

4.2. Variability in Near-Surface Shear and φ_ε

Considerable scatter occurs in φ_ε along with variability in calculated near-surface shear (Figures 11 and 20). While the variability may have been due to changes in the state of mixing (e.g., Smyth et al., 2019) and related variability in R_f, other processes could have contributed. When winds were less than 3 m s^{-1}, the vorticity of surface gravity waves may have contributed to the variability in φ_ε. Laboratory and numerical experiments in which low amplitude surface gravity waves, ~0.01–0.015 m, were superimposed on either quiescent or turbulent flows indicate that temperature stratification can be rapidly eroded (Dai et al., 2010) and that near-surface vorticity from the gravity waves can augment near-surface turbulence (Tsai et al., 2015). However, in the numerical experiments of Tsai et al. (2015), the turbulence was anisotropic whereas we observed isotropic turbulence. Lien et al.'s (2008) analysis in a fetch limited oceanographic site indicates that wind-driven shear is larger and extends more deeply than that due to Stokes drift. In contrast, Laxague and Zappa (2020) illustrate time varying shear from wave orbital velocities that exceeds that from Stokes drift. Our data during morning heating and light winds cannot evaluate the exact processes operating. It does show the critical control of ζ on φ_ε with variability in φ_ε due to the presence of ripples versus small amplitude surface waves (Text S1, Table S1, Figure S4).

Langmuir cells have been posited to increase near-surface dissipation rates and to form once winds reach 3 m s^{-1}. We did not observe these larger scale features. However, as winds begin to increase above 3 m s^{-1}, Langmuir circulations of 4–10 cm horizontal scale may form (Veron & Melville, 2001). Their observations showed ε to quickly increase from ~5×10^{-6} to 10^{-5} m^2 s^{-3} as wind speed increased from 2 to 3 m s^{-1}, similar to our observations mid-day on DOY 200 (Text S2, Figure S5). Our calculations indicate shear of order 0.1 m s^{-1} when winds reached 3 m s^{-1}. McWilliams et al. (1997) illustrate that Langmuir cells decrease near-surface shear, but it is not clear how shear would be moderated in the Langmuir circulations. High frequency internal waves were also present near the surface mid-day DOY 200 (Figures 8 and S5), as on other days. These moderated near surface stratification and would also moderate shear and strain (Alford & Pinkel, 2000; MacIntyre et al., 1999). Microstructure profiles taken during heating conditions showed temperature instabilities similar to those from Kelvin-Helmholtz billows

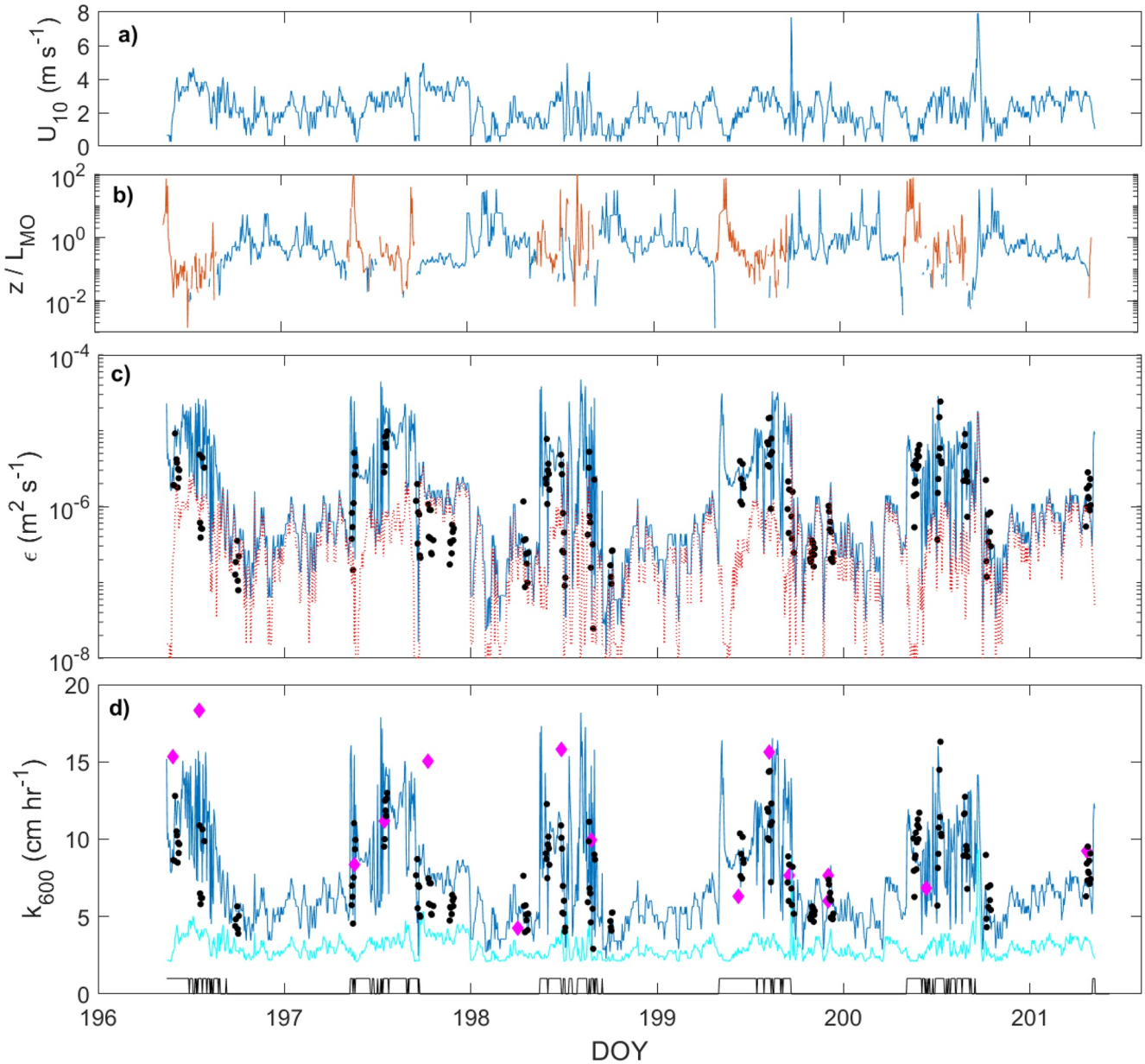

Figure 19. Time series of (a) U_{10}; (b) z/L_{MO} for heating (orange) and cooling (blue, note sign is negative under cooling); (c) Dissipation rates from SCAMP (black dots) and computed from time series temperature and meteorological data following MOST as $\varepsilon = \varepsilon_s (1 + 1/R_f\, z/L_{MO})$ using the temporally varying R_f calculated from Re_β (see Figure 11) during heating and $\varepsilon = \varepsilon_s (1 + 0.5\ |z/L_{MO}|^{2/3})^{3/2}$ (Wyngaard & Coté, 1971) during cooling (blue line), ε_s (red line); k_{600ch} obtained from chamber measurements (magenta diamonds) and computed from the surface renewal model using calculated ε from SCAMP (black dots) and using dissipation rates computed from MOST (ε) as in panel (c) (blue line), and using the wind based model of Cole and Caraco (1998, cyan). Black lines at the bottom of panel d indicate periods of heating. Depths for calculations are 0.15 m as in Figures 11 and 13. Close agreement of k_{600} from chamber measurements with k_{600} from the surface renewal model provides further support for our modeling approaches.

in the actively mixing layer (Figure 1). These imply the near-surface turbulence was induced by shear as could occur with these interacting processes. In the analysis of the data from mid-day DOY 200, the range of ζ was restricted to 0.2 to 0.6 and variability in φ_ε resulted from changes in Re_β particularly as wind speeds increased and stratification was weakened (Text S2 and S3, Figure S5). Determining whether the variability φ_ε and in near-surface shear resulted from the onset of Langmuir circulations requires additional field experiments during heating conditions coupled with those that characterize shear and strain in the near-surface internal wave field.

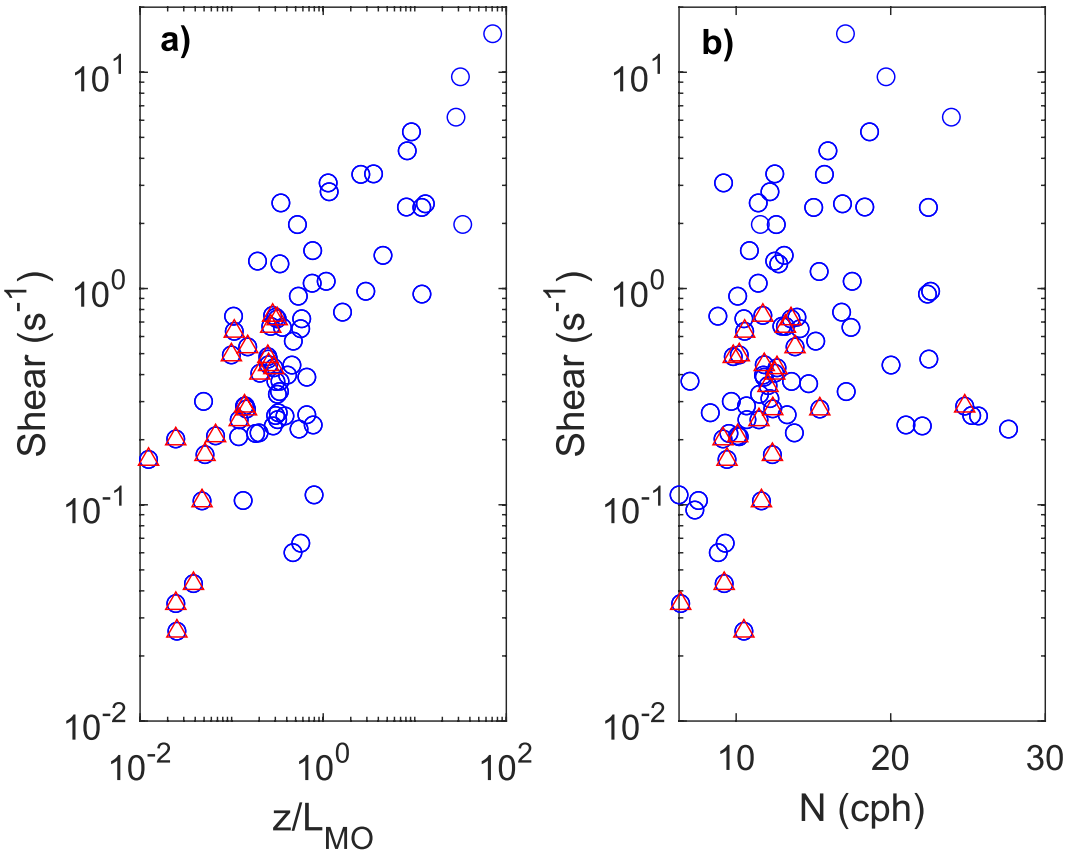

Figure 20. Increase in shear calculated from φ_ε and R_f relative to (a) z/L_{MO} where z is 0.15 m and (b) to buoyancy frequency N (cph). Red circles indicate shear for $U_{10} \geq 3$ m s^{-1}. For reference, N = 10 cph is equivalent to $\log_{10}(N^2) = -3.5$ and N = 30 cph is equivalent to $\log_{10}(N^2) = -2.56$.

4.3. Combined Influence of Changes in Wind Speed and Stratification on ε

The effects of the changing dynamics on ε are illustrated in Figure 21. While the highest dissipation rates were found for wind speeds above 2.5 m s^{-1}, they were more consistently high when β_* was highest as occurred by late morning (Figure 21a). Dissipation rates were also higher when N was 10–12 cph, as occurred when the enhanced shear with rising winds reduced near-surface stratification despite the considerable heating (Figure 21b). The highest dissipation rates occurred when z/L_{MO} was between 0.1 and 1, higher than expected from wind shear alone but in the range with only a modest increase from β_* (Figure 21c). Highest dissipation rates occurred when R_f was least, following our model that φ_ε increases with $1/R_f$ z/L_{MO} (Figure 21d). As R_f is calculated from Re_β following Monismith et al. (2018), these results are not independent. However, the calculations of φ_ε from the SCAMP data in Figure 11 do not depend on R_f and illustrate the five to 10 fold increases in φ_ε relative to law of the wall scaling for $0.1 < z/L_{MO} < 1$.

Thus, when taken together, this composite analysis explains the dynamics during heating and light winds that lead to the high variability in φ_ε as z/L_{MO} begins to exceed 0.1. That is, with ongoing heating and increased shear, be it from wind alone or enhanced by the oscillatory motions of surface waves, heat is mixed downwards reducing the stratification. The buoyancy Reynolds number increases, as does the turbulent Froude number, indicating the energy supplied exceeds that required for mixing. Hence, values of R_f decrease to low values leading to the enhancement of φ_ε and of ε (Figures 11 and 21).

4.4. Gas Transfer Velocities, Dissipation Rates, and Mixing Efficiency During Heating

Gas transfer velocities for wind speeds from 0.5 to 3.5 m s^{-1}, calculated using the surface renewal model and ε computed from the microstructure data, ranged from 5 to 16 cm hr^{-1} under heating, similar to predictions from

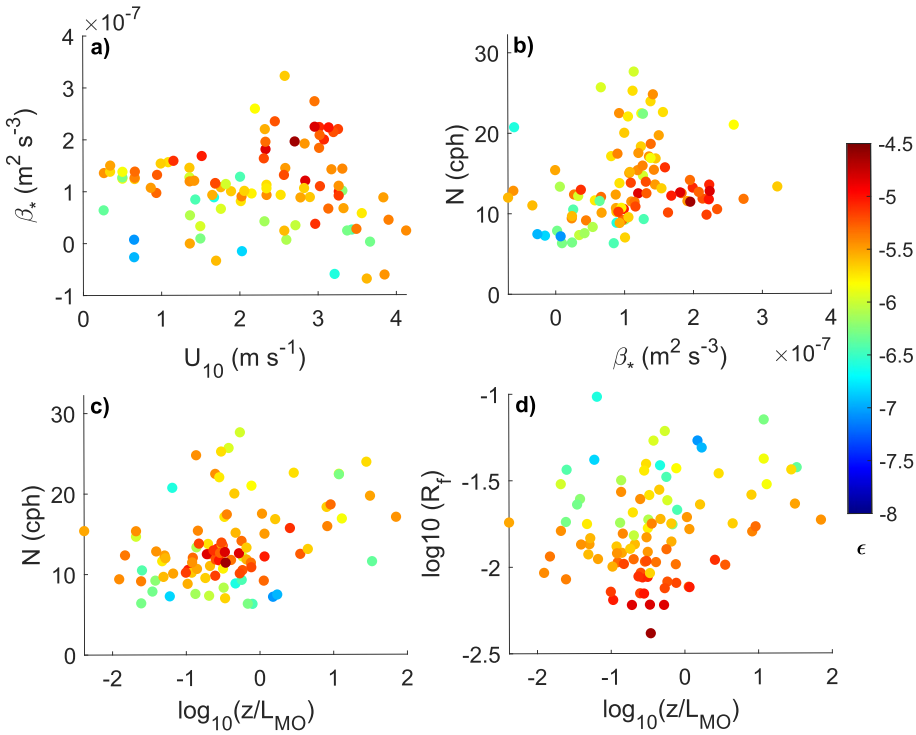

Figure 21. Scatter plots showing variation of ϵ during heating as it depends on (a) U_{10} and effective buoyancy flux (β_*); (b) β_* and buoyancy frequency N; (c) z/L_{MO} and N; and (d) z/L_{MO} and R_f with R_f calculated following Monismith et al. (2018).

the estimates of ϵ modeled using MOST and three to five times higher than predictions from wind-based models (Cole & Caraco, 1998) (Figure 19d) and Wanninkhof (2014) (data not shown). Values of k_{600ch} obtained with chamber measurements during heating, 5–18 cm hr^{-1}, were similar to model results obtained using the time varying estimates of R_f. Thus, this study provides multiple lines of evidence that R_f in water immediately below the air-water interface varies, is lower than the critical value of 0.2, and contributes to enhanced ϵ and k_{600} relative to expected values from law of the wall scaling.

The elevated dissipation rates for the low wind speeds reported under heating result because φ_ε increases with $1/R_f \cdot z/L_{MO}$ (Figure 11). That is, as the influence of wind shear decreases relative to heating, the near-exponential increase in φ_ε compensates for the lower expected shear stress at light winds (Figures 11, 14f, and 18). Using the inverse of R_f in modeling, the rate of increase in φ_ε with z/L_{MO} is more rapid than in prior models (Figure 11). In fact, once z/L_{MO} exceeds 1, φ_ε is nearly an order of magnitude higher using the R_f model resulting from our data than Grachev et al. (2013). Dissipation rates exceeded buoyancy flux (b) in the upper 0.25 m typically by an order of magnitude. The vertical transport of buoyancy, calculated as $T = g/\rho\ K_z\ d\rho/dz$, is similar to b. Calculations of $R_f = b/(b+\varepsilon)$ or as $b/(b + T+\varepsilon)$ were similar, due to the appreciably higher dissipation rates. This analysis supports the typical assumption for stable atmospheric boundary layers of the near equality of φ_ε and φ_m and resultant low values of R_f, such as we calculated from the microstructure data (Figure 10c). Given the near equality of φ_ε to φ_m, where $\varphi_m = (\kappa z/u_{*w})\ dU/dz$, the increased φ_ε in this study relative to earlier ones implies a larger velocity gradient just below the water surface than in the boundary layer studies over land and ice and below the air-water interface in the temperate lake during fall cooling (Grachev et al., 2013, 2015; Tedford et al., 2014). The high shear and accompanying turbulence production, and limited mixing, explain the high dissipation rates we observed and may also explain the similar high values found by Sutherland et al. (2016) and Hughes et al. (2020a) in diurnal warm layers.

Our observations support research indicating that variable and low mixing efficiencies can occur for shear-induced mixing of stably stratified waters (Monismith et al., 2018; Shih et al., 2005; Walter et al., 2014). In fact, as the buoyancy Reynolds number from which R_f is computed exceeded 500 throughout the actively mixing layer and at times within the diurnal thermocline (Figure 9), these results indicate that rates of mixing within much

of the upper mixed layer may be lower than predicted using a fixed Γ of 0.2 despite elevated dissipation rates (Brainerd & Gregg, 1993; Gregg et al., 2018). Monismith et al. (2018) suggested the incidence of active mixing would be found more frequently near boundaries, such as the ocean bottom. Here, we illustrate $R_f < 0.17$ below the air-water interface during heating. Further, Monismith et al. (2018) suggested the incidence would be greater if the length scales of mixing were less than the Ozmidov scale, $L_O = (\varepsilon/N^3)^{1/2}$. For the ~100 observations we have under heating in the upper 0.25 m, $L_T \leq L_O$ in all but 4 cases. As L_T decreased below 0.2 m, $L_T/L_O < 0.1$. Thus, the turbulence was isotropic despite N ranging from 5 to 30 cph. The turbulent Froude number (Fr_T) ranged from 1 to 7 for $L_T < 0.2$ m for all but two data points. Fr_T ranged from 1.5 to 7 for $L_T < 0.08$ m, and ε exceeded 10^{-6} m^2 s^{-3} when $Fr_T > 2.5$ for all but a few data points (Figure S1). These values of Fr_T are indicative of isotropic turbulence where R_f is expected to be less than 0.17 (Ivey & Imberger, 1991; Monismith et al., 2018; Shih et al., 2005). Similarly, during heating $L_o/\kappa{\cdot}z > ¼$, indicating the criteria in Gregg et al. (2018) for R_f declining with increasing Re_β was also met. Thus, these observations support the growing literature illustrating conditions in which R_f and Γ are less than critical values and provide a basis for more accurate calculations of the coefficient of eddy diffusivity and gas transfer velocities in the surface layer of lakes and oceans.

If elevated dissipation rates under light winds and heating as reported here occur in diverse water bodies, inclusion of both physical and biological processes that modify near-surface stratification is warranted in regional carbon models. The diel cycles we report for a tropical reservoir are similar to those from other inland tropical (Augusto-Silva et al., 2019; MacIntyre et al., 2002, 2014; Yang et al., 2019), temperate and boreal (Heiskanen et al., 2014; Pernica et al., 2014), and arctic water bodies (MacIntyre et al., 2009, 2018), the Gulf of Aqaba (Dunckley et al., 2012), and several oceanographic sites (Brainerd & Gregg, 1993; McGillis et al., 2004; Shay & Gregg, 1986). For comparison, maximal net heat flux, the sum of the surface fluxes and net short wave radiation, reached or approached 700 W m^{-2} at Balbina *R* (Figure 2). When wind stress at the oceanic sites was similar to what we observed, dissipation rates in near-surface layers reached values of 10^{-6} m^2 s^{-3} and occasionally exceeded 10^{-5} m^2 s^{-3}, similar to our observations (Brainerd & Gregg, 1993; Shay & Gregg, 1986; Sutherland et al., 2016). In the study in the equatorial Pacific, the mean shear stress and u_{*_w} were twice what we observed, and the diel patterns in w_* were similar (McGillis et al., 2004). Similar to our study, gas transfer velocities reached 12.5 cm hr^{-1} during the heating period and were independent of wind speed despite the slightly higher winds of ~6 m s^{-1}. The relation of their binned values of k_{660}, where 660 is the Schmidt number for CO_2 at 20°C in seawater, to wind speed at 10 m is: $k_{660} = 8.2 + 0.014U_{10}^3$. Calculations using U_{10} for our study, and including a Schmidt number correction, predict k_{600} consistently between 9 and 10 cm hr^{-1}, similar to our maximum likelihood estimates under heating, but do not capture the variability associated with the processes leading to variability in R_f (Figure 21). In short, the magnitudes of heat fluxes and wind shear we observed at Balbina R. have similarly been observed at inland water sites and oceanographic sites during light to moderate winds. Where data are available, near-surface dissipation rates during heating and light winds have exceeded 10^{-6} m^2 s^{-3}. These between site comparisons indicate that enhancement of dissipation rates and gas transfer velocities in the near-surface layer under heating and light winds may be ubiquitous and that including the coupled processes moderating near-surface stratification in regional carbon models is essential.

5. Conclusions

Our estimates of rates of dissipation of turbulent kinetic energy under light winds and heating advance calculation and understanding of gas transfer velocities (*k*). In particular, increased shear and decreased mixing efficiency were found to lead to enhanced gas transfer velocities under light winds and heating. Values of *k* were 4–5 times higher than computed from wind-based models. Striking features include the high dissipation rates in the upper 0.25 m associated with the formation of the diurnal thermocline and further increases in dissipation rates as wind speeds increased and stratification weakened in the upper 0.25 m and increased at depths immediately below. Near-surface dissipation rates computed from the microstructure data were an order of magnitude higher during heating than cooling for wind speeds less than 4 m s^{-1} and had a greater dependency on surface buoyancy flux than on wind speed. The buoyancy Reynolds number was typically elevated above 500 during the heating period, and the mean flux Richardson number was 0.04, indicating the turbulence was actively growing and isotropic. Thus, more of the energy input by the wind was dissipated rather than used for mixing. The rapid changes in near-surface stratification and in dissipation rates in response to subtle changes in heating, cooling, wind speed and direction are distinctive feature of our results from Balbina Reservoir. The widespread occurrence of diurnal

thermoclines in lakes and oceans plus our evidence for elevated dissipation rates and gas transfer velocities under these conditions call for a reevaluation of fluxes of trace gases in regional carbon models under light winds.

Conflict of Interest

The authors declare no conflicts of interest relevant to this study.

Data Availability Statement

Data have been deposited at the National Center for Ecological Analysis and Synthesis Knowledge. Network for Biocomplexity long-term archive. Data are available at the following links: https://knb.ecoinformatics.org/view/doi:10.5063/F1B56H50, https://knb.ecoinformatics.org/view/doi%3A10.5063/8G8J46, https://knb.ecoinformatics.org/view/doi%3A10.5063/0Z71P4.

Acknowledgments
We thank B. R. Forsberg for logistic support, A. T. Crowe, M. J. Czikowsky, and E. W. Tedford for contributions to data processing and graphics, J. A. Tota for the loan of the Kipp and Zonen radiometer, and A. Trindade and J. B. Rocha for assistance in the field. We thank the owner and staff of Restaurante do Mirandinha for logistic support. We thank the three anonymous reviewers for helpful comments. Field work was supported in part by Ministério da Ciência Tecnologia CNPq/LBA-Edital.68/2013, processo 458036/ 2013-8, and CNPq - Universal processo 482004/2012-6 to B. R. Forsberg, by NASA Terrestrial Ecology Grant NNX10AB66G to John M. Melack and Sally MacIntyre, and U.S. NSF DEB 0919603 to Sally MacIntyre. Post-graduate scholarships were provided to JHFA by CNPQ and CAPES. Additional support for data analysis and manuscript preparation was provided by NASA Contract NNX17AK49G and the US National Science Foundation Division of Environmental Biology, grant number 1753856 to John M. Melack and Sally MacIntyre, and NSF DEB 0919603 and ANS 1737411 to Sally MacIntyre.

References

Alford, M. H., & Pinkel, R. (2000). Observations of overturning in the thermocline: The context of ocean mixing. *Journal of Physical Oceanography*, *30*, 805–832. https://doi.org/10.1175/1520-0485(2000)030<0805:oooitt>2.0.co;2

Amaya, D. J., Miller, A. J., Xie, S.-P., & Kosaka, Y. (2020). Physical drivers of the summer 2019 North Pacific marine heatwave. *Nature Communications*, *11*, 1903. https://doi.org/10.1038/s41467-020-15820-w

Anis, A., & Moum, J. N. (1992). The superadiabatic surface layer of the ocean during convection. *Journal of Physical Oceanography*, *22*, 1221–1227. https://doi.org/10.1175/1520-0485(1992)022<1221:TSSLTO>2.0.co;2

Anis, A., & Moum, J. N. (1995). Surface wave-turbulence interactions: Scaling $\epsilon(z)$ near the sea-surface. *Journal of Physical Oceanography*, *25*, 2025–2045. https://doi.org/10.1175/1520-0485(1995)025<2025:SWISNT>2.0.co;2

Augusto-Silva, P. B., MacIntyre, S., Rudorff, C., Cortés, A., & Melack, J. M. (2019). Stratification and mixing in large floodplain lakes along the lower Amazon River. *Journal of Great Lakes Research*, *45*, 61–72. https://doi.org/10.1016/j.jglr.2018.11.001

Barbosa, P. M., Melack, J. M., Farjall, V. F., Amaral, J. H. F., Scofield, V., & Forsberg, B. R. (2016). Diffusive methane fluxes from Negro, Solimoes, and Madeira rivers and fringing lakes in the Amazon basin. *Limnology Oceanography*, *61*(S1), S210–S237. https://doi.org/10.1002/lno.10358

Batchelor, G. K. (1959). Small-scale variation of convected quantities like temperature in turbulent fluid. Part 1. General discussion and the case of small conductivity. *Journal of Fluid Mechanism*, *5*, 113–133.

Bouffard, D., & Boegman, L. (2013). A diapycnal diffusivity model for stratified environmental flows. *Dynamics of Atmospheres and Oceans*, *61–62*, 14–34. https://doi.org/10.1016/j.dynatmoce.2013.02.002

Bouffard, D., & Wuest, A. J. (2019). Convection in lakes. *Annual Review of Fluid Mechanics*, *51*, 189–215. https://doi.org/10.1146/annurev-fluid-010518-040506

Brainerd, K. E., & Gregg, M. C. (1993). Stratification and turbulence in oceanic surface mixed layer. 1. Observations. *Journal of Geophysical Research*, *98*, 22645–22656. https://doi.org/10.1029/93jc02297

Brainerd, K. E., & Gregg, M. C. (1995). Surface mixed and mixing layer depths. *Deep-Sea Research*, *42*, 1521–1543. https://doi.org/10.1016/0967-0637(95)00068-h

Brumer, S. E., Zappa, C. J., Blokquist, B. W., Fairall, C. W., Cifuentes_Lorenzen, A., Edson, J. B., et al. (2017). Wave-related Reynolds number parameterizations of CO_2 and DMS transfer velocities. *Geophysical Research Letters*, *44*, 9865–9875. https://doi.org/10.1002/2017GL074979

Chou, S.-H., Atlas, D., & Yeh, E.-N. (1986). Turbulence in a convective marine atmospheric boundary layer. *Journal of the Atmospheric Sciences*, *43*, 5472–5564. https://doi.org/10.1175/1520-0469(1986)043<0547:tiacma>2.0.co;2

Cole, J. J., & Caraco, N. F. (1998). Atmospheric exchange of carbon dioxide in a low-wind oligotrophic measured by the addition of SF_6. *Limnology & Oceanography*, *43*, 647–656. https://doi.org/10.4319/lo.1998.43.4.0647

Crill, P. M., Bartlett, K. B., Wilson, J. O., Sebacher, D. I., Harris, R. C., Melack, J. M., et al. (1988). Tropospheric methane from an Amazonian floodplain lake. *Journal of Geophysics Research*, *93*, 1564–1570.

Csanady, G. T. (2001). *Air-sea interaction: Laws and mechanisms*. Cambridge University Press.

Czikowsky, M. J., MacIntyre, S., Tedford, E. W., Vidal, J., & Miller, S. D. (2018). Effects of wind and buoyancy on carbon dioxide distribution and air-water flux of a stratified temperate lake. *Journal of Geophysics Research: Biogeosciences*, *123*, 2305–2322. https://doi.org/10.1029/2017JG004209

Dai, D., Qiao, F., Sulisz, W., Han, L., & Babanin, A. (2010). An experiment on the nonbreaking surface-wave-induced vertical mixing. *Journal of Physical Oceanography*, *40*, 2180–2188. https://doi.org/10.1175/2010JPO4378.1

D'Asaro, E. A. (2014). Turbulence in the upper-ocean mixed layer. *Annual Review Marine Science*, *6*, 101–115. https://doi.org/10.1146/annurev-marine-010213-135138

Dunckley, J. F., Koseff, J. R., Steinbuck, J. V., Monismith, S. G., & Genin, A. (2012). Comparison of mixing efficiency and vertical diffusivity models from temperature microstructure. *Journal of Geophysical Research*, *117*, C1008. https://doi.org/10.1029/2012JC007967

Endoh, T., Matsuno, T., Yoshikawa, Y., & Tsutsumi, E. (2014). Estimates of the turbulent kinetic energy budget in the oceanic convective boundary layer. *Journal of Oceanography*, *70*, 81–90. https://doi.org/10.1007/s10872-013-0215-3

Fairall, C. W., Bradley, E. F., Rogers, D. P., Edson, J. B., & Young, G. S. (1996). Bulk parameterization of air-sea fluxes for tropical ocean-global atmosphere coupled-ocean atmosphere response experiment. *Journal of Geophysical Research*, *101*, 3747–3764. https://doi.org/10.1029/95jc03205

Frölicher, T. L., Fischer, E. M., & Gruber, N. (2018). Marine heatwaves under global warming. *Nature*, *560*, 360–364. https://doi.org/10.1038/s41586-018-0383-9

Gargett, A. E., Osborn, T. R., & Nasmyth, P. W. (1984). Local isotropy and the decay of turbulence in a stratified fluid. *Journal of Fluid Mechanics*, *144*, 231–280. https://doi.org/10.1017/s0022112084001592

Grachev, A. A., Andreas, E. L., Fairall, C. W., Guest, P. S., & Persson, P. O. G. (2007). SHEBA flux-profile relationships in the stable boundary layer. *Boundary-Layer Meteorology*, *124*, 315–333. https://doi.org/10.1007/s10546-007-9177-6

Grachev, A. A., Andreas, E. L., Fairall, C. W., Guest, P. S., & Persson, P. O. G. (2013). The critical Richardson number and limits of applicability of local similarity theory in the stable boundary layer. *Boundary-Layer Meteorology*, *147*, 51–82. https://doi.org/10.1007/s10546-012-9771-0

Grachev, A. A., Andreas, E. L., Fairall, C. W., Guest, P. S., & Persson, P. O. G. (2015). Similarity theory based on the Dougherty-Ozmidoz length scale. *Quarterly Journal of the Royal Meteorological Society*, *141*, 1485–1856. https://doi.org/10.1002/qj.2488

Gregg, M. C., D'Asaro, E. A., Riley, J. J., & Kunze, E. (2018). Mixing efficiency in the ocean. *Annual Review Marine Science*, *10*, 443–473. https://doi.org/10.1146/annurev-marine-121916-063643

Hamilton, S., Sippel, S., & Melack, J. M. (1995). Oxygen depletion and carbon dioxide and methane production in waters of the Pantanal wetland of Brazil. *Biogeochemistry*, *30*, 115–141. https://doi.org/10.1007/bf00002727

Hara, T., & Sullivan, P. P. (2014). Wave boundary layer turbulence over surface waves in a strongly forced condition. *Journal of Physical Oceanography*, *45*, 868–883. https://doi.org/10.1175/JPO-D-14_0116.1

Heiskanen, J. J., Mammarella, I., Haapanala, S., Pumpanen, J., Vesala, T., MacIntyre, S., & Ojala, A. (2014). Effects of cooling and internal wave motions on gas transfer coefficients in a boreal lake. *Tellus B: Chemical and Physical Meteorology*, *66*, 22827. https://doi.org/10.3402/tellusb.v66.22827

Hicks, B. B. (1975). A procedure for the formulation of drag and bulk transfer coefficients over water. *Boundary-Layer Meteorology*, *8*, 515–524. https://doi.org/10.1007/bf02153568

Holleman, R., Geyer, W., & Ralston, D. (2016). Stratified turbulence and mixing efficiency in a salt wedge estuary. *Journal of Physical Oceanography*, *46*, 1769–1783. https://doi.org/10.1175/JPO-D-15-0193.1

Hughes, K. G., Moum, J. N., & Schroyer, E. L. (2020a). Evolution of the velocity structure in the diurnal warm layer. *Journal of Physical Oceanography*, *50*, 615–631. https://doi.org/10.1175/JPO-D-19-0207.1

Hughes, K. G., Moum, J. N., & Schroyer, E. L. (2020b). Heat transport through diurnal warm layers. *Journal of Physical Oceanography*, *50*, 2885–2905. https://doi.org/10.1175/JPO-D-20-0079.1

Imberger, J. (1985). The diurnal mixed layer. *Limnology & Oceanography*, *30*, 737–770. https://doi.org/10.4319/lo.1985.30.4.0737

Imberger, J., & Boashash, B. (1986). Application of the Wigner-Ville distribution to temperature-gradient microstructure: A new technique to study small-scale variations. *Journal of Physical Oceanography*, *16*, 1997–2012. https://doi.org/10.1175/1520-0485(1986)016<1997:aotwdt>2.0.co;2

Imberger, J., & Ivey, G. N. (1991). On the nature of turbulence in a stratified fluid. Part II. Application to lakes. *Journal of Physical Oceanography*, *21*, 659–680. https://doi.org/10.1175/1520-0485(1991)021<0659:otnoti>2.0.co;2

Ivey, G. N., Bluteau, C. E., & Jones, N. L. (2018). Quantifying diapycnal mixing in an energetic ocean. *Journal of Geophysical Research: Oceans*, *123*, 346–357. https://doi.org/10.1002/2017JC013242

Ivey, G. N., & Imberger, J. (1991). On the nature of turbulence in a stratified fluid. Part I: The energetics of mixing. *Journal of Physical Oceanography*, *21*, 650–658. https://doi.org/10.1175/1520-0485(1991)021<0650:otnoti>2.0.co;2

Jähne, B., Munich, K. O., Bosinger, R., Dutzi, A., Huber, W., & Libner, P. (1987). On the parameters influencing air-water gas exchange. *Journal of Geophysical Research*, *92*, 1937–1950.

Jellison, R. J., & Melack, J. M. (1993). Meromixis in hypersaline Mono Lake, California. 1. Stratification and vertical mixing during the onset, persistence, and breakdown of meromixis. *Limnology & Oceanography*, *38*, 1008–1019. https://doi.org/10.4319/lo.1993.38.5.1008

Jonas, T., Stips, A., Eugster, W., & Wuest, A. (2003). Observations of a quasi shear-free lacustrine convective boundary layer: Stratification and its implications on turbulence. *Journal of Geophysical Research*, *108*, 3328. https://doi.org/10.1029/2002JC001440

Katul, G., Mammarella, I., Grönholm, T., & Vesala, T. (2018). A structure function model recovers the many formulations for air-water gas transfer velocity. *Water Resources Research*, *54*(9), 5905–5920. https://doi.org/10.1029/2018WR022731

Kemenes, A. (2006). *Emissão de metano e gás carbônico pela Hidrelétrica de Balbina. PhD Thesis* (p. 98). Instituto Nacional de Pesquisa da Amazônia.

Kemenes, A., Forsberg, B. R., & Melack, J. M. (2011). CO_2 emissions from a tropical hydroelectric reservoir (Balbina, Brazil). *Journal of Geophysics Research Biogeoscience*, *116*, G03004. https://doi.org/10.1029/2010jg001465

Kirkpatrick, M. P., Williamson, N., Armfield, S. W., & Zecevic, V. (2019). Evolution of thermally stratified open channel flow after removal of the heat source. *Journal of Fluid Mechanics*, *876*, 356–412. https://doi.org/10.1017/jfm.2019.543

Lamont, J. C., & Scott, D. S. (1970). Eddy cell model of mass transfer into the surface of a turbulent liquid. *AIChE Journal*, *16*(4), 513–519. https://doi.org/10.1002/aic.690160403

Laxague, N. J. M., & Zappa, C. J. (2020). Observations of mean and wave orbital flows in the ocean's upper centimeters. *Journal of Fluid Mechanics*, *887*, A10. https://doi.org/10.1017/jfm.2019.1019

Leibovich, S. (1983). The form and dynamics of Langmuir circulations. *Annual Review of Fluid Mechanics*, *15*, 391–427. https://doi.org/10.1146/annurev.fl.15.010183.002135

Lien, R.-C., Sanford, B., & Tsai, W.-T. (2008). Observations of turbulence mixing and vorticity in a littoral surface boundary layer. *Journal of Physical Oceanography*, *38*, 648–669. https://doi.org/10.1175/2007jpo3469.1

Lombardo, C., & Gregg, M. C. (1989). Similarity scaling of viscous and thermal dissipation in a convecting surface boundary layer. *Journal of Geophysical Research*, *94*, 6273–6284. https://doi.org/10.1029/jc094ic05p06273

MacIntyre, S. (2021a). *Meteorological data: Balbina R. 15 - 20 July 2013 (5 minute averaged)*. Knowledge Network for Biocomplexity. https://doi.org/10.5063/F1B56H50

MacIntyre, S. (2021b). *Temperature data, Balbina reservoir, Brazil, 15-20 July 2013, 10 second data*. Knowledge Network for Biocomplexity. https://doi.org/10.5063/8G8J46

MacIntyre, S. (2021c). *Temperature-gradient microstructure data; Balbina reservoir, Brazil, 1-20*. Knowledge Network for Biocomplexity. https://doi.org/10.5063/0Z71P4

MacIntyre, S., Amaral, J. H. F., Barbosa, P. M., Cortés, A., Forsberg, B. R., & Melack, J. M. (2019). Turbulence and gas transfer velocities in sheltered flooded forests of the Amazon Basin. *Geophysical Research Letters*, *46*, 9628–9636. https://doi.org/10.1029/2019gl083948

MacIntyre, S., Bastviken, D., Arneborg, L., Crow, A. T., Karlsson, J., Andersson, A., et al. (2021). Turbulence in a small boreal lake: Consequences for air-water gas exchange. *Limnology & Oceanography*, *66*, 827–854. https://doi.org/10.1002/lno.11645

MacIntyre, S., Crowe, A. T., Cortés, A., & Arneborg, L. (2018). Turbulence in a small arctic pond. *Limnology & Oceanography*, *63*, 2337–2358. https://doi.org/10.1002/lno.10941

MacIntyre, S., Flynn, K. M., Jellison, R., & Romero, J. R. (1999). Boundary mixing and nutrient fluxes in Mono Lake, California. *Limnology & Oceanography*, *44*, 512–529. https://doi.org/10.4319/lo.1999.44.3.0512

MacIntyre, S., Jonsson, A., Jansson, M., Aberg, J., Turney, D. E., & Miller, S. D. (2010). Buoyancy flux, turbulence, and the gas transfer coefficient in a stratified lake. *Geophysical Research Letters*, *37*, L24604. https://doi.org/10.1029/2010GL044164

MacIntyre, S., Romero, J. R., & Kling, G. W. (2002). Spatial-temporal variability in surface layer deepening and lateral advection in an embayment of Lake Victoria, East Africa. *Limnology & Oceanography*, *47*, 656–671. https://doi.org/10.4319/lo.2002.47.3.0656

MacIntyre, S., Romero, J. R., Silsbe, G. M., & Emery, B. M. (2014). Stratification and horizontal exchange in Lake Victoria, East Africa. *Limnology & Oceanography*, *59*, 1805–1838. https://doi.org/10.4319/lo.2014.59.6.1805

MacIntyre, S., Wanninkhof, R., & Chanton, J. P. (1995). Trace gas exchange across the air-water interface in freshwater and coastal marine environments. In P. A. Matson, & R. C. Harriss (Eds.), *Methods in Ecology, biogenic trace gases: Measuring emissions from soil and water* (pp. 52–97). Blackwell Science.

Mammarella, I., Nordbo, A., Rannik, U., Haapanala, S., Levula, J., Laakso, H., et al. (2015). Carbon dioxide and energy fluxes over a small lake in southern Finland. *Journal of Geophysics Research Biogeoscience*, *120*, 1296–1314. https://doi.org/10.1002/2014JG002873

McGillis, W. R., Edson, J. B., Hare, J. E., & Fairall, C. W. (2001). Direct covariance air-sea CO_2 fluxes. *Journal of Geophysical Research*, *106*(C8), 16729–16745. https://doi.org/10.1029/2000JC000506

McGillis, W. R., Edson, J. B., Zappa, C. J., Ware, J. D., McKenna, S. P., Terray, E. A., et al. (2004). Air-sea CO_2 exchange in the equatorial Pacific. *Journal of Geophysical Research*, *109*, C08S02. https://doi.org/10.1029/2003JC002256

McWilliams, J. C., Sullivan, P. P., & Moeng, C. H. (1997). Langmuir turbulence in the ocean. *Journal of Fluid Mechanics*, *334*, 1–30. https://doi.org/10.1017/S0022112096004375

Melack, J. M., Hess, L. L., Gastil, M., Forsberg, B. R., Hamilton, S. K., Lima, I. B. T., & Novo, E. M. L. M. (2004). Regionalization of methane emissions in the Amazon basin with microwave remote sensing. *Global Change Biology*, *10*, 530–544. https://doi.org/10.1111/j.1365-2486.2004.00763.x

Monin, A. S., & Obukhov, A. M. (1954). Basic laws of turbulent mixing in the surface layer of the atmosphere. *Trans. Geophys. Inst. Akad. Nauk. SSSR*, *24*(151), 163–187.

Monismith, S. G., Koseff, J. R., & White, B. L. (2018). Mixing efficiency in the presence of stratification: When is it constant? *Geophysical Research Letters*, *45*, 5627–5634. https://doi.org/10.1029/2018GL077229

Moum, J. N., Farmer, D. M., Smyth, W. D., Armi, L., & Vagle, S. (2003). Structure and generation of turbulence at interfaces strained by internal solitary waves propagating shorward over the continental shelf. *Journal of Physical Oceanography*, *33*, 2093–2112. https://doi.org/10.1175/1520-0485(2003)033<2093:sagota>2.0.co;2

O'Reilly, C. M., Gray, D. K., Sharma, S., Hampton, S. E., Read, J. S., Rowley, R. J., et al. (2015). Global patterns in lake warming from 1985-2009. *Geophysical Research Letters*, *42*(10), 773–781. https://doi.org/10.1002/2015GL066235

Osborn, T. R. (1980). Estimates of the local-rate of vertical diffusion from dissipation measurements. *Journal of Physical Oceanography*, *102*, 83–89. https://doi.org/10.1175/1520-0485(1980)010<0083:eotlro>2.0.co;2

Osborn, T. R., & Cox, C. S. (1972). Oceanic fine structure. *Geophysical Fluid Dynanics*, *3*, 321–345. https://doi.org/10.1080/03091927208236085

Pernica, P., Wells, M., & MacIntyre, S. (2014). Persistent weak thermal stratification inhibits mixing in the epilimnion of north-temperate Lake Opeongo, Canada. *Aquatic Sciences*, *76*, 187–201. https://doi.org/10.1007/s00027-013-0328-1

Peters, H., Gregg, M. C., & Toole, J. M. (1988). On the parameterization of equatorial turbulence. *Journal Geophysics Research*, *93*, 1199–1218.

Polsenaere, P., Deborde, J., Detandt, G., Vidal, L. O., Perez, M. A. P., Marieu, V., & Abril, G. (2013). Thermal enhancement of gas transfer velocity of CO_2 in an Amazon floodplain lake revealed by eddy covariance measurements. *Geophysical Research Letters*, *40*, 1–7. https://doi.org/10.1002/grl.50291

Price, J. F., Weller, R. A., & Pinkel, R. (1986). Diurnal cycling: Observations and models of the upper ocean response to diurnal heating, cooling, and wind mixing. *Journal of Geophysical Research*, *91*, 8411–8427. https://doi.org/10.1029/jc091ic07p08411

Raymond, P. A., Hartmann, J., Lauerwald, R., Sobek, S., McDonald, C., Hoover, M., et al. (2013). Global carbon dioxide emissions from inland waters. *Nature*, *503*, 355–359. https://doi.org/10.1038/nature12760

Richey, J. E., Melack, J. M., Aufdenkampe, A. K., Ballester, V. M., & Hess, L. (2002). Outgassing from Amazonian rivers and wetlands as a large tropical source of atmospheric CO_2. *Nature*, *416*, 617–620. https://doi.org/10.1038/416617a

Ruddick, B., Anis, A., & Thompson, K. (2000). Maximum likelihood spectral fitting: The Batchelor spectrum. *Journal of Atmospheric and Oceanic Technology*, *17*, 1541–1555. https://doi.org/10.1175/1520-0426(2000)017<1541:mlsftb>2.0.co;2

Sanz Rodrigo, J., & Anderson, P. S. (2013). Investigation of the stable-atmospheric boundary layer at Halley Antarctica. *Boundary-Layer Meteorology*, *148*, 517–539. https://doi.org/10.1007/s10546-013-9831-0

Shay, T. J., & Gregg, M. C. (1986). Convectively driven turbulent mixing in the upper ocean. *Journal of Physical Oceanography*, *16*, 1777–1798. https://doi.org/10.1175/1520-0485(1986)016<1777:cdtmit>2.0.co;2

Shcherbina, A. Y., D'Asara, E. A., Harcourt, R. R., & Harcourt, R. (2019). Rain and sun create slippery layers in the Eastern Pacific Fresh Pool. *Oceanography*, *32*(2), 98–107. https://doi.org/10.5670/oceanog.2019.217

Shih, L. H., Koseff, J. R., Ivey, G. N., & Ferziger, J. H. (2005). Parameterization of turbulent fluxes and scales using homogeneous sheared stably stratified turbulence simulations. *Journal of Fluid Mechanics*, *525*, 193–214. https://doi.org/10.1017/s0022112004002587

Sjöblom, A., & Smedman, A.-S. (2002). The turbulent kinetic energy budget in the marine atmospheric surface layer. *Journal of Geophysical Research*, *107*, 3142. https://doi.org/10.1029/2001JC001016

Smyth, W. D., Nash, J. D., & Moum, J. N. (2019). Self-organized criticality in geophysical turbulence. *Scientific Reports*, *9*, 3747. https://doi.org/10.1038/s41598-019-39869-w

Soloviev, A. V., & Lukas, R. (2006). *The near-surface layer of the ocean*. Springer.

Soloviev, A. V., Lukas, R., & Hacker, P. (2001). An approach to parameterization of the oceanic turbulent boundary layer in the western Pacific warm pool. *Journal of Geophysical Research*, *106*, 4421–4435. https://doi.org/10.1029/2000jc900154

Soloviev, A. V., Vershinsky, N. V., & Bezverchnii, V. A. (1988). Small-scale turbulence measurements in the thin surface layer of the ocean. *Deep-Sea Research*, *35*, 1859–1874. https://doi.org/10.1016/0198-0149(88)90113-6

St. Laurent, L., & Merrifield, S. (2017). Measurements of near-surface turbulence and mixing from autonomous ocean gliders. *Oceanography*, *30*(2), 116–125. https://doi.org/10.5670/oceanog.2017.231

Steinbuck, J. V., Stacey, M. T., & Monismith, S. G. (2009). An evaluation of χ_T estimation techniques: Implications for Batchelor fitting and ε. *Journal of Atmospheric and Oceanic Technology*, *26*, 1652–1662. https://doi.org/10.1175/2009JTECHO611.1

Sutherland, G., Marie, L., Reverdin, G., Christensen, K. H., Brostrom, G., & Ward, B. (2016). Enhanced turbulence associated with the diurnal jet in the ocean surface boundary layer. *Journal of Physical Oceanography*, *46*, 3051–3067. https://doi.org/10.1175/JPO-D-15-0172.1

Tedford, E. W., MacIntyre, S., Miller, S. D., & Czikowsky, M. J. (2014). Similarity scaling of turbulence in a temperate lake during fall cooling. *Journal of Geophysics Research: Oceans*, *119*, 4689–4713. https://doi.org/10.1002/2014JC010135

Tennekes, H., & Lumley, J. L. (1972). *A first course in turbulence*. MIT Press.

Terray, E. A., Donelan, M. A., Agrawal, Y. C., Drennan, W. M., Kahma, K. K., Williams, A. J., III, et al. (1996). Estimates of kinetic energy dissipation under breaking waves. *Journal of Physical Oceanography*, *26*, 792–807. https://doi.org/10.1175/1520-0485(1996)026<0792:eokedu>2.0.co;2

Thorpe, S. A. (2007). *An introduction to ocean turbulence*. Cambridge University Press.

Tsai, W.-T., Chen, S.-M., & Lu, G.-H. (2015). Numerical evidence of turbulence generated by nonbreaking surface waves. *Journal of Physical Oceanography*, *45*, 174–180. https://doi.org/10.1175/jpo-d-14-0121.1

Tsai, W.-T., Lu, G.-H., Chen, J.-R., Dai, A., & Phillips, W. R. C. (2017). On the formation of coherent vortices beneath nonbreaking free-propagating surface waves. *Journal of Physical Oceanography*, *47*, 533–543. https://doi.org/10.1175/JPO-D-16-0242.1

Turner, J. S. (1973). *Buoyancy effects in fluids*. Cambridge University Press.

Turney, D. E., & Banerjee, S. (2013). Air-water gas transfer and near-surface motions. *Journal of Fluid Mechanics*, *733*, 588–624. https://doi.org/10.1017/jfm.2013.435

Venayagamoorthy, S., & Koseff, J. R. (2016). On the flux Richardson number in stably stratified turbulence. *Journal of Fluid Mechanics*, *798*, R1. https://doi.org/10.1017/jfm.2016.340

Veron, F., & Melville, W. K. (2001). Experiments on the stability and transition of wind-driven water surfaces. *Journal of Fluid Mechanics*, *446*, 25–65. https://doi.org/10.1017/S0022112001005638

Walter, R. K., Squibb, M. E., Woodson, C. B., Koseff, J. R., & Monismith, S. G. (2014). Stratified turbulence in the nearshore coastal ocean: Dynamics and evolution in the presence of internal bores. *Journal of Geophysical Research: Oceans*, *119*, 8709–8730. https://doi.org/10.1002/2014JC010396

Wang, B., Liao, Q., Fillingham, J. H., & Bootsma, H. A. (2015). On the coefficients of small eddy and surface divergence models for the air-water gas transfer velocity. *Journal of Geophysical Research: Oceans*, *120*, 2129–2146. https://doi.org/10.1002/2014JC010253

Wanninkhof, R. (1992). Relationship between gas exchange and wind speed over the ocean. *Journal of Geophysical Research*, *97*, 7373–7381. https://doi.org/10.1029/92jc00188

Wanninkhof, R. (2014). Relationship between wind speed and gas exchange over the ocean. *Limnology and Oceanography: Methods*, *12*, 351–362. https://doi.org/10.4319/lom.2014.12.351

Ward, B. (2006). Near-surface ocean temperature. *Journal of Geophysics Research: Oceans*, *111*, C02004. https://doi.org/10.1029/2004JC002689

Wuest, A., & Lorke, A. (2003). Small-scale hydrodynamics in lakes. *Annual Review of Fluid Mechanics*, *35*, 373–412. https://doi.org/10.1146/annurev.fluid.35.101101.161220

Wyngaard, J., & Coté, O. (1971). The budgets of turbulent kinetic energy and temperature variance in the atmospheric surface layer. *Journal of the Atmospheric Sciences*, *28*, 190–201. https://doi.org/10.1175/1520-0469(1971)028<0190:tbotke>2.0.co;2

Xenopoulos, M. A., & Schlinder, D. W. (2001). The environmental control of near-surface thermoclines in boreal lakes. *Ecosystems*, *4*, 699–707. https://doi.org/10.1007/s10021-001-0038-8

Yamamoto, S., Alcauskas, J. B., & Crozier, T. E. (1976). Solubility of methane in distilled water and seawater. *Journal of Chemistry Engineering Data*, *21*, 78–80. https://doi.org/10.1021/je60068a029

Yang, P., Fong, D. A., LoYat-Man, E., & Monismith, S. G. (2019). Vertical mixing in a shallow tropical reservoir. *Limnology*, *20*, 279–296. https://doi.org/10.1007/s10201-019-00577-z

Yeates, P. S., & Imberger, J. (2004). Pseudo two-dimensional simulations of internal and boundary fluxes in stratified lakes and reservoirs. *International Journal of River Basin Management*, *1*, 1–23.

Zappa, C. J., McGillis, W. R., Raymond, P. A., Edson, J. B., Hintsa, E. J., Zemmelink, H. J., et al. (2007). Environmental turbulent mixing controls on air-water gas exchange in marine and aquatic systems. *Geophysical Research Letters*, *34*, L10601. https://doi.org/10.1029/2006GL028790